Search for same-sign dilepton signatures with the ATLAS detector

Master's thesis
by
Inga Rún Helgadóttir

Supervisor:
Monika Wielers

LUND UNIVERSITY

Department of Physics
Lund, 2013

Abstract

This thesis presents the work I did for the inclusive search for anomalous production of same charge lepton-pairs, originating from the collision point, at $\sqrt{s} = 8$ TeV with the ATLAS detector at the LHC using the 2012 data. I optimized the selection criteria for isolated electrons and muons, calculated the so-called "fake factors" and "fake factor" systematic uncertainties for the muon selection. The fake-factor is used to estimate the contribution in the region of interest due to muons coming from secondary vertices, i.e. background muons. Furthermore I extracted limits of the cross-section of new sources of isolated, same-sign leptons originating from the collision point. The isolation criteria and the limits are used in the paper on the search for anomalous production of same-sign lepton-pairs originating from the collision point, which will be published soon.

I found that for this analysis the best background rejection while still achieving a good signal efficiency is accomplished by using isolation criteria based on both calorimeter and tracking information.

The muon fake factors are calculated in a data-driven way using muon pairs having the same charge. The fake factors obtained using the new selection criteria for isolated muon tracks are higher than when the isolation criteria from the previous analysis is used, but the new criteria also accepts substantially more true same-sign muons originating from the collision point, resulting in a lower ratio of muons originating from secondary vertices to muons originating from the collision point in the region of interest.

As we are working on publishing the results it was not possible to analyse the region of interest because of internal ATLAS restrictions. Hence it is not known whether the data agrees with the predictions from known physics processes. If no excess is found in the number of lepton pairs I will put limits on the cross section of new resonances. At the moment I am only allowed to calculate the expected limits.

Acknowledgements

First of all I would like to thank my supervisor, Monika Wielers, for being the best supervisor I could have wished for, and Anthony Hawkins for being like a second supervisor to me. Both were always taking their time to explain things to me and help me when I was stuck in my analysis.

My thanks go also to Kenji Hamano for suggesting I should do the limit setting and for sharing his program code and knowledge on the issue.

Special thanks go to my parents and to all who helped babysit Arnór Bragi in the last weeks before hand in of this thesis, otherwise I could not have finished in time.

And finally I want to thank all the staff and students in the experimental high energy physics division for making my stay at the division really enjoyable!

Inga Rún

Contents

Chapter 1

Introduction

We do have a remarkable theory, called the Standard Model, that successfully describes almost all experimental particle physics results so far. However, there are still some big questions unanswered about the universe. For example what is the universe made of? It has been shown that all the particles we know only make up about 5% of the universe. So what is the rest? Do there exist extra dimensions? And can all particles and forces in the universe be explained by a single theory of everything? These are intriguing questions. Such questions have driven many into studying physics, including me.

For my master thesis I looked for signs of new physics beyond the Standard Model (SM). I participated in the search for non-Standard Model production of two prompt[1], isolated[2] leptons[3] with the same electric charge. It is an interesting search since many beyond Standard Model (BSM) models include decays to same charge lepton-pairs, while it is a rare process within the SM. Hence this search is well suited for looking for signs of non-SM processes quite model independently, and can be used to put limits on and even exclude certain BSM models.

I optimized the isolation cuts, i.e. found the cuts that had the best rejection of non-isolated leptons and jets misidentified as leptons, while still keeping most of the isolated ones. I calculated a scale factor called the "fake factor" for the muon selection which is used to estimate the contamination of non-prompt muons in the region of interest. I also calculated the systematic uncertainties associated with the fake factor. I will put exclusion limits on the fiducial[4] cross-section of non-SM physics resulting in prompt same-sign lepton pairs if no excess in lepton pairs will be found. It was not possible to analyse the region of interest because of internal ATLAS restrictions when this dissertation was handed in, hence for the observed limits, presented in the preliminary results in this thesis, the numbers used are based on educated guesses assuming no new physics occurs. The isolation cuts and limit setting will be used in the paper on this subject to be published in early 2014.

This chapter contains a short introduction to particle physics and descriptions of the Large Hadron Collider and the ATLAS detector. The reconstruction and identification of electrons and muons in ATLAS and Monte Carlo event generation is also discussed since they are relevant to the work done for this thesis. The last section in this chapter

[1]Prompt leptons are leptons created at the collision point.

[2]Leptons that are isolated from other particles in the detector.

[3]The two leptons can either have the same mother particle or come from the decays of different particles. Lepton pairs can also be called dileptons.

[4]A fiducial region is a well defined region in phase-space in which the detector operates with high efficiency.

contains a brief overview of the software used in the analysis.

In chapter 2 I will explain the main steps of the prompt same-sign dilepton analysis and in chapters 3, 4 and 5 I will discuss my contribution to the analysis and show the results. Specifically my optimization studies of the isolation cuts are summarized in chapter 3, the muon fake factors and corresponding systematic uncertainties in chapter 4 and the limit setting in chapter 5. Chapter 6 summarizes the conclusions of my work.

1.1 The Standard Model and beyond

Particle physics studies the physics of fundamental particles and forces. The main underlying theory is called the *Standard Model* (SM) [49]. It describes all known particles and the strong, weak and electromagnetic forces. The SM is a quantum field theory based on gauge symmetries. Its gauge group is $SU(3)_c \times SU(2)_W \times U(1)_Y$, where the group $SU(3)_c$ represents Quantum Cromodynamics (QCD), the theory describing the strong force, and $SU(2)_W \times U(1)_Y$ represents the electroweak theory, which unifies the electromagnetic and the weak force. According to the SM there are 12 elementary fermions, 12 gauge bosons and one scalar Higgs boson. The fermions all have antiparticles, particles with the same mass but opposite charge. The antineutrino has opposite chirality[5] to the neutrino but still they might be identical particles.

Fermions are particles with half-integer spin and they must obey the Pauli Exclusion Principle, i.e. no two fermions can occupy the same quantum space. Bosons have integer spin and do not follow this rule. The Higgs is a scalar particle implying it has no spin.

The SM contains two types of fundamental fermions: quarks and leptons. The leptons come in three families, or flavors: electron, muon and tau. Each family consists of one negatively charged particle (e^-, μ^-, τ^-) and one neutral particle (ν_e, ν_μ, ν_τ). The neutrinos interact only via the weak force, hence they are very difficult to detect. Electrons, muons and taus interact mainly via the electromagnetic force. Originally it was believed that neutrinos were massless but now it has been shown that they have small but non-vanishing mass [41]. The mass of the other leptons is known with high precision and it increases from family to family, the electron family being the lightest one.

The six quarks are grouped into three families, with the lightest and stable ones in the first: (u, d), (c, s) and (t, b). The u, c, t quarks have electric charge $+2e/3$ and the d, s, b quarks have charge $-e/3$, where e is the elementary electric charge. The quarks also have a color charge, *red*, *green* or *blue*, and interact via the strong force. The quark masses are not known with high precision because of color confinement. This is the phenomenon that manifests itself by the fact that color charged particles, like the quarks, cannot be isolated and are bound together into colorless hadrons. Three quarks, one with each color charge, form the so-called baryons and a quark and a anti-quark form the so-called mesons.

All ordinary stable matter in the universe contains only quarks and leptons of the first generation since they are the lightest. The fermion masses can be seen in table 1.1. Neutrino masses are non-vanishing, since neutrino oscillations are observed, but they are not well known and are therefore not included in the table. Using tritium decay, it has been shown that their masses are less than 2 eV/c^2.

The remaining Standard Model elementary particles are bosons. The SM gauge bosons

[5]Chirality is determined by whether the particle transforms in a right or left-handed representation of the Poincaré group. For massless particles it is the same as helicity.

Table 1.1: Fermion masses in the SM. Numbers are taken from the Particle Data Group [30].

1^{st} family		2^{nd} family		3^{rd} family	
name	mass (MeV/c^2)	name	mass (GeV/c^2)	name	mass (GeV/c^2)
u	$2.3^{+0.7}_{-0.5}$	c	1.275 ± 0.025	t	$173.07 \pm 0.52 \pm 0.72$
d	$4.8^{+0.5}_{-0.3}$	s	0.095 ± 0.005	b	4.18 ± 0.03[1]
e	0.511	μ	0.106	τ	1.777

[1] $\overline{\text{MS}}$ scheme (modified minimal subtraction).

are force carriers. The photon carries the electromagnetic force. It is massless and has no charge. Hence photons are non-selfinteracting, giving the electromagnetic force infinite range. Electromagnetic interactions bind together the nucleus and the electrons forming atoms. $W^{\pm}$ and Z^0 bosons carry the weak force. They are heavy and self-interacting, resulting in a very short range of the weak force, $\sim 10^{-3}$ fm. The weak interaction is responsible for both radioactive decay and nuclear fusion. 8 gluons carry the strong force. The gluons are massless but contain color charge. They can therefore self-interact, which limits the strong force to short ranges, < 1 fm. The strong force binds quarks together forming hadrons and is also responsible for binding protons and neutrons together to form atomic nuclei. The last boson is the Higgs boson. It has mass around 125 GeV [23, 35], is spinless and has no electric or color charge. The Higgs boson is a quantum excitation of the Higgs field, which is a weak isospin ($SU(2)$) doublet and has therefore four components. The vacuum expectation value of the Higgs field gives masses to all massive Standard Model particles through the Higgs mechanism. Three of the Higgs field components interact with the W and Z bosons and generate their masses. The remaining part is what we "see" as a 125 GeV Higgs boson, which interacts with fermions via Yukawa couplings causing them to acquire mass. The electric charge group $U(1)_{em}$ remains unbroken after spontaneous symmetry breaking and hence the photon remains massless [31].

Table 1.2: The Standard Model gauge bosons

Gauge boson	**Force and range**	**Mass** (GeV/c^2)	**Gauge group**	**Charge**
photon (γ)	Electromagnetism infinite range	0	unbroken $U_{em}(1)$ combination of $SU(2) \times U(1)$	Electrically neutral
$W^{\pm}$	Weak force	80.4	broken combination	W and Z have weak charge[1]
Z	$\sim 10^{-3}$ fm	91.2	of $SU(2) \times U(1)$	W has electric charge ± 1
8 gluons (g)	Strong force < 1 fm	0	$SU(3)_c$	Color charge

[1] The weak hypercharge is a conserved quantum number unifying weak interactions with electromagnetic interactions.

The SM is a very successful theory and describes very well the physics measured in the particle physics experiments. However, there are some problems showing that it is not complete [47]. For example, the SM does not explain the asymmetry between matter and antimatter in the universe, neutrino masses, dark matter and dark energy. And moreover it does not include the fourth fundamental force, gravity.

There are a lot of models trying to build up a more general theory. Some of these models predict new particles which should be detectable at the energy scale accessible by the Large Hadron Collider (LHC). Part of these models include processes which produce

prompt same charge leptons, a process which is rare within the Standard Model, and therefore provides a way of looking for new processes, quite model independently, above a low Standard Model background. Processes resulting in two prompt same sign leptons are for example predicted by supersymmetry [29], Higgs triplet models [13], the little Higgs model [18] and left-right symmetric models [53].

- Supersymmetry is probably the best known of these models. It is a proposed symmetry relating fermions and bosons. According to it, all known particles have a superpartner of opposite statistics[6], making the superpartner of a fermion a boson and vice versa. If supersymmetry is true, a hadron collider like the LHC is optimal for producing gluinos and squarks, the superpartners of gluons and quarks, which could decay to same sign lepton pairs. For example the dominant gluino decay mode is $\tilde{g} \to q\bar{q}\tilde{\chi}_1^{\pm}$, where $\tilde{\chi}_1^{\pm}$ is the lightest chargino. The chargino can then decay in the following way: $\tilde{\chi}_1^{\pm} \to W^{\pm}\tilde{\chi}_1^0 \to l^{\pm}\nu\tilde{\chi}_1^0$ where $\tilde{\chi}_1^0$ is the lightest neutralino, the lightest supersymmetric particle, and $W^{\pm}$ boson can be either a real or a virtual particle (see figure 1.1).

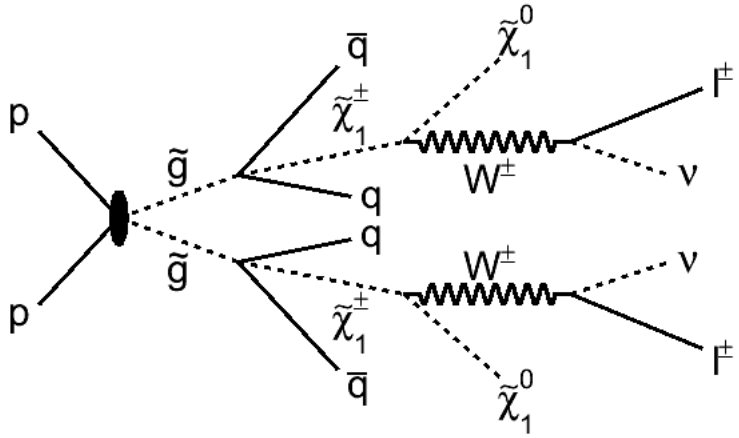

Figure 1.1: A same charge dilepton signature of supersymmetry: the decay of gluinos to a same sign lepton pair, neutrinos and neutralinos.

- The Higgs triplet models are models that can explain the neutrino mass generation. A $SU(2)$ triplet of scalar particles with hypercharge[7] $Y = 2$ is added to the SM Lagrangian. This would allow neutrinos to gain mass via the vacuum expectation value (vev) of a neutral Higgs boson[8]. These models predict a doubly charged Higgs boson $H^{\pm\pm}$. A possible decay channel would be $pp \to H^{++}H^{--} \to l^+l^+l^-l^-$ (see figure 1.2).

- The little Higgs model is a model based on electroweak symmetry breaking. It is an alternative to supersymmetry. It predicts that each SM particle has a TeV scale "partner" of same statistics (opposite to supersymmetry) which cancel the quadratically divergent contributions to the Higgs mass. A possible decay channel would be through a $H^{\pm\pm}$ like in figure 1.2.

[6]Fermions follow Fermi-Dirac statistics while bosons obey Bose-Einstein statistics.
[7]Hypercharge is a quantum number relating the strong interactions of the $SU(3)$ model.
[8]The expectation value of the Higgs field in the vacuum, i.e. 246 GeV [31].

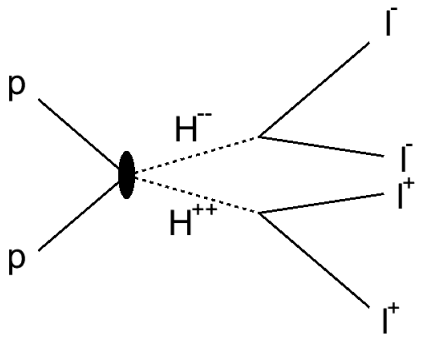

Figure 1.2: A same charge dilepton signature of Higgs triplet models: $pp \to H^{++}H^{--} \to l^+l^+l^-l^-$

- Parity is broken in electroweak interactions and the $W^\pm$ bosons couple only to left-handed quarks and leptons. The left-right symmetric models have an additional gauge group $SU(2)_R$ which would predict the existence of right handed W bosons. These models actually predict 3 new gauge bosons ($W_R^\pm, Z_R$) and 3 heavy neutrinos $N_{R,e}, N_{R,\mu}, N_{R,\tau}$. As shown in ref. [53], left-right symmetry can be spontaneously broken to give a chiral low energy theory, which is the Standard Model, and it also connects the small observed neutrino masses to the breaking of left-right symmetry via the see-saw mechanism[9]. A possible same-sign dilepton signature is the decay of a right handed W boson to a lepton and a heavy neutrino where the neutrino decays to a lepton and two jets, $W_R \to l^\pm N \to l^\pm l^\pm jj$.

1.2 LHC

The Large Hadron Collider (LHC) is the world's biggest particle accelerator with a circumference of 27 km. It is located at the research facility CERN[10] near Geneva and is a superconducting hadron collider.

The particle beams are in two separate beam pipes, at absolute vacuum[11], with opposite sign magnetic fields. That is necessary since both beams consist of protons. The magnetic field strength in the beam pipe is 8.33 T and it guides the proton beams around the accelerator. Dipole magnets are used for the bending of the beam. Liquid helium at 1.9K is used to cool the magnets. Along the accelerator there are special radiofrequency (RF) cavities. They are used to group the particles into tight bunches and accelerate them. Just before bunch crossing, quadrupole magnets squeeze the particles closer together to increase the chances of collisions.

But before getting to the LHC ring, protons are accelerated in the CERN accelerator complex. At injection to the LHC ring, the protons have been accelerated to 450 GeV. The maximum beam energy in the LHC is 7 TeV but in 2012 the accelerator was operated with 4 TeV beam energies. Figure 1.3 shows the current LHC injector chain.

[9]The see-saw mechanism is a generic model used to understand the relative sizes of observed neutrino masses, of the order of eV, compared to those of quarks and charged leptons, of the order of $10^6 - 10^{11}$ eV/c^2.

[10]Acronym derived from *Conseil Européen pour la Recherche Nucléaire* and it was retained although the name was changed to the current *Organisation Européenne pour la Recherche Nucléaire*

[11]I.e. apart from the proton bunches there is no matter, and hence no pressure, inside the beam pipes.

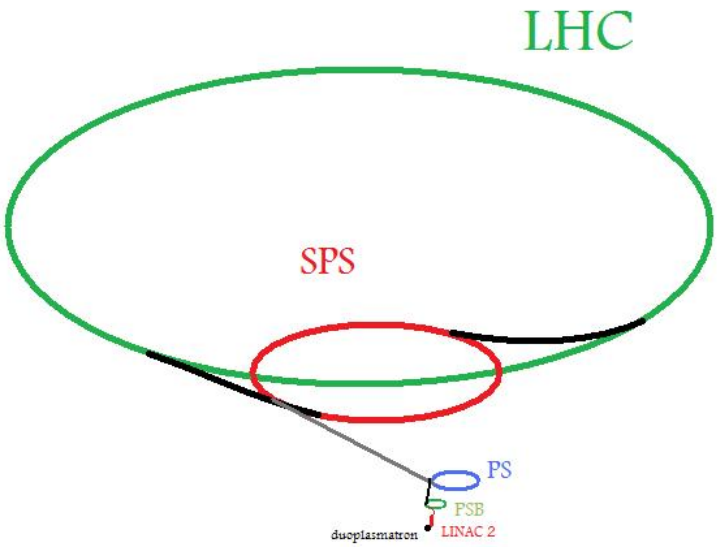

Figure 1.3: A schematic diagram of the LHC injector chain. The proton acceleration starts at the Linear accelerator 2 (Linac2). The particles are then injected to the Proton Synchrotron Booster (PSB), the Proton Syncrotron (PS), and the Super Proton Syncrotron (SPS) before reaching the LHC [5].

When designing particle accelerators a key parameter is the center-of-mass energy, denoted by $\sqrt{s}$. Higher center-of-mass energy means higher energy available for probing new physics beyond the Standard Model. To get high center-of-mass energy you need to be able to accelerate particles almost to the speed of light. The maximal achievable $\sqrt{s}$ in the LHC is 14 TeV (7 TeV from each beam).

The proton is not an elementary particle. It consists of two up quarks, one down quark and gluons. Quarks and gluons are commonly denoted as partons. The hard scattering processes within the LHC occur between two partons in the hadrons. Therefore the energy available for creating new particles is not the whole center-of-mass energy of the hadrons, but the center-of-mass energy of the interacting partons. That value can vary a lot, making the LHC good for the discovery of new particles of unknown mass because it is possible to probe different energy regions at the same time. Another advantage of hadron colliders above lepton colliders is much lower synchrotron radiation since it is inversely proportional to the fourth power of the mass of the accelerated particles. Hence higher center-of-mass energies can be achieved.

Most collisions happening in the LHC are not interesting from a discovery perspective as they do not come from a hard (head-on) collision and only low energy particles are produced. Therefore luminosity is an important parameter. Luminosity is the number of particles per unit area per unit time, expressed in units of $\mathrm{cm}^{-2}\ \mathrm{s}^{-1}$. The interaction rate is the multiple of the inelastic proton-proton cross section, σ_{inel}, and the luminosity, $\mathcal{L}$ or

$$R = \sigma_{\mathrm{inel}} \times \mathcal{L} \tag{1.2.1}$$

A great effort has been put into obtaining as high as possible luminosity. 2012's peak luminosity was $\approx 7.5 \times 10^{33}\ \mathrm{cm}^{-2}\ \mathrm{s}^{-1}$ [59], and at $\sqrt{s} = 8$ TeV the inelastic proton-proton cross section is ≈ 73 mb [58][59], hence the maximum number of events per second was around:

$$N_{\mathrm{evt}} = 7.5 \times 10^{33} \times 73 \times 10^{-3} \times 10^{-24} = 550 \quad \text{million/s} \tag{1.2.2}$$

The integral of the delivered luminosity over time is called integrated luminosity. It is a measurement of the collected data and is usually given in units of inverse barns (b) where one barn is equal to 10^{-24} cm^2. Not all of the delivered luminosity is recorded by the experiments at LHC and not all of the recorded luminosity is suited for physics analysis, for example because of detector timing errors[12] and because of the time it takes to increase the voltage in the detector after a beam becomes stable. Figure 1.4 shows the cumulative luminosity versus time, delivered to, recorded by the ATLAS experiment, and certified to be good quality data. ATLAS data quality was excellent in 2012 with all sub-detectors showing more than 99% efficiency. As a result, a record integrated luminosity of over 21.3 fb^{-1} of data had been collected by December 2012. Figure 1.5 shows the online luminosity[13] in 2010 - 2012.

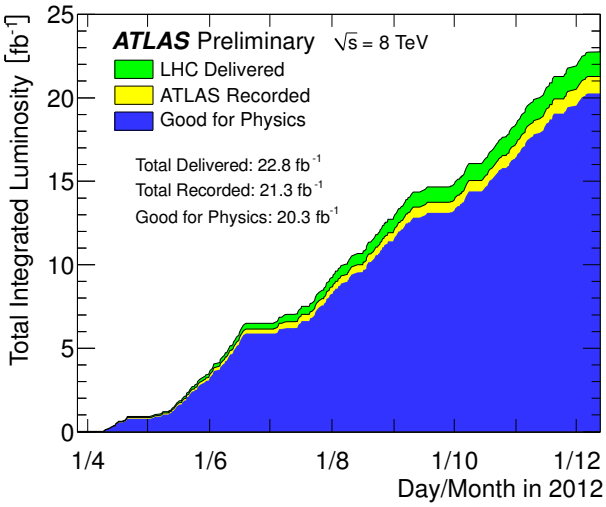

Figure 1.4: Cumulative luminosity versus time delivered to (green), recorded by ATLAS (yellow), and certified to be good quality data (blue) during stable beams and for pp collisions at 8 TeV centre-of-mass energy in 2012. From [59].

Table 1.3 lists the nominal LHC beam parameters. In 2012 some of the parameters were different. For example, the collision energy was $\sqrt{s} = 8$ TeV instead of $\sqrt{s} = 14$ TeV, the number of bunches per beam were 1374 instead of 2808 and the bunch spacing was 50 ns instead of the nominal value of 25 ns [45]. However the average number of interactions per crossing in 2012 was 20.7 [59] which already exceeded the design value of 19.02.

The investment to design, build, calibrate and understand the accelerator and the detectors and to analyse the results resulted in the discovery of the Higgs particle. The discovery of an unknown boson was announced on 4th of July 2012 by both the ATLAS and CMS experiments (Ref. [23] and[35]), and it is now confirmed to be almost certainly the Standard Model Higgs [25, 26].

In the 2013-2015 shutdown the LHC is being upgraded to run at design collision energy, $\sqrt{s} = 13 - 14$ TeV. The restart is scheduled in early 2015.

The main LHC experiments, ATLAS, CMS, ALICE and LHCb, are situated at the four interaction points around the LHC accelerator. ATLAS and CMS are general-purpose detectors and they are the biggest LHC experiments. It is vital to have more

[12]The read out information can not be mapped to the right bunch crossing.

[13]The online luminosity is the luminosity measured in real time and is the measure of the amount of collisions produced by the LHC.

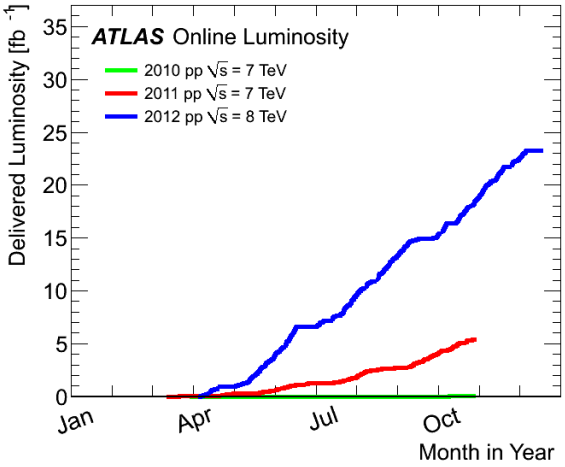

Figure 1.5: Cumulative online luminosity versus day delivered to ATLAS during stable beams and for p-p collisions. This is shown for 2010 (green), 2011 (red) and 2012 (blue) running. From [59].

Table 1.3: LHC beam, machine and storage ring parameters relevant for design luminosity[34].

		Value at injection	Value at collision
Proton energy	[GeV]	450	7000
Relativistic γ		479.6	7461
Number of particles per bunch		1.15×10^{11}	
Number of bunches		2808	
Circulating beam current	[A]	0.582	
Stored energy per beam	[MJ]	23.3	362
Peak luminosity in IP1 (ATLAS)	[$\mathrm{cm}^{-2}\mathrm{s}^{-1}$]	-	1.0×10^{34}
Events per bunch crossing		-	19.02
Synchrotron radiation power per ring	[W]	6.15×10^{-2}	3.6×10^{3}
Energy loss per turn	[eV]	1.15×10^{-1}	6.71×10^{3}
Ring circumference	[m]	26,658.883	
Number of dipole magnets		1232	
Length of dipole magnets	[m]	14.3	
Field of dipole magnets	[T]	0.535	8.33
Bending radius	[m]	2,803.95	
Revolution frequency	[kHz]	11.245	
RF frequency	[MHz]	400.8	

than one experiment to be able to cross check the results in case of a discovery of a new particle. ALICE is dedicated to heavy ion physics and LHCb studies the b quark to investigate the matter-antimatter asymmetry.

More information about the LHC can be found in references [34, 39].

1.3 ATLAS

The ATLAS[14] detector is a general purpose detector which means that it has a very good hermeticity (4π coverage), precise tracking information and calorimetric energy reconstruction capabilities and good particle identification capabilities. It is designed to perform precision tests of SM parameters, search for the SM Higgs and search for physics beyond the Standard Model. It is 46 meter long, over 25 meter in diameter and weights about 7,000 tons, which makes it the biggest particle detector ever built. It utilizes ∼100 million read-out channels to record the signal from the particles produced in the collisions [7, 21].

1.3.1 Detector layout

The ATLAS detector is built symmetrically around the interaction point. It has a series of concentric detector systems around the interaction point. Going outwards from the interaction point, a particle passes the inner tracking detector, the calorimeters and the muon spectrometer. Each system is dedicated to a different measurement of the particle properties.

The ATLAS coordinate system is defined such that the interaction point is the origin. The z-axis is parallel with the beam direction, the positive x-axis is defined as pointing from the interaction point to the center of the LHC ring and the positive y-axis is defined as pointing upwards. The azimuthal angle ϕ is measured around the beam axis, and the polar angle θ is the angle from the beam axis. The pseudorapidity is defined as $\eta = -\ln \tan(\theta/2)$ and is often used instead of θ. It is a convenient unit to use since in a hadron collider the number of particles produced per unit of η is the same for all η. The transverse momentum p_{T}, the transverse energy E_{T}, and the missing transverse energy $E_{\mathrm{T}}^{\mathrm{miss}}$ are defined in the x-y plane unless stated otherwise, so $p_{\mathrm{T}} = \sqrt{p_x^2 + p_y^2}$ and so on. The distance ΔR in the pseudorapidity-azimuthal angle space is defined as $\Delta R = \sqrt{\Delta\eta^2 + \Delta\phi^2}$ [21].

ATLAS is designed for precision physics up to $\eta < 2.5$.

Inner Detector

The Inner Detector is contained in a 2 T magnetic field and provides pattern recognition, excellent momentum resolution and both primary and secondary vertex measurements for charged particles in the pseudorapidity range $|\eta| < 2.5$. It consists of the silicon pixel detector (pixel), the semiconductor tracker (SCT) and the transition radiation tracker (TRT) [7, 21]. The three layers of the pixel detector have a very fine track resolution of 0.014×0.115 mm^2. The SCT has four cylindrical double layers in the barrel and two times 9 disks in the forward region. It can record the positions of charged particles to an intrinsic accuracy of 0.017×0.580 mm^2. The TRT is a straw tube detector. The straw tubes are 4 mm in diameter with an anode wire in the center having a diameter of 0.03 mm. It does not provide information on η but can make precision measurement of 0.17 mm in ϕ. Lighter particles radiate more photons then heavier particles when they pass through the TRT and thus similar behaving particles can be distinguished. The pion for example is much heavier than the electron and radiates therefore much less.

[14] **A T**oroidal **L**HC **A**pparatu**S**

Calorimeters

Calorimeters measure the energy and position of incoming particles (although only the position of muons). They are the only detectors that can detect neutral as well as charged particles. The neutrinos go undetected but a measurement of the missing transverse energy, $E_{\mathrm{T}}^{\mathrm{miss}}$, is provided. To measure the energy of the incoming particles they are stopped in the detector medium and the deposited energy is measured. The particles are made go through some dense material, creating a cascade of secondary particles which are absorbed by the detector. Calorimetric measurements are also crucial to particle identification, serving to distinguish electrons and photons from hadron jets by analysing the shower shape, and also helping to identify hadronic decays of tau leptons.

The ATLAS calorimeters [7, 21] consist of a number of sampling detectors[15] with full ϕ-symmetry and coverage around the beam axis. There are a barrel, end-cap and forward calorimeters which cover the range $|\eta| < 4.9$. Innermost is the electromagnetic calorimeter (ECAL), which measures the energy of electrons and photons, and outside of it is the hadronic calorimeter (HCAL), which measures the energy of hadrons. The total thickness of the calorimeter system is at least 10 hadron absorption lengths over the whole acceptance region, which has been shown to be sufficient to absorb hadrons completely. Together with the large η-coverage, this thickness will also ensure a good $E_{\mathrm{T}}^{\mathrm{miss}}$ measurement, which is important for many physics signatures and in particular for Supersymmetry particle searches.

The ECAL consists of a barrel and end cap calorimeters. It uses lead absorbers and a liquid-Argon ionization medium. Each part of the calorimeter is contained in a cryostat at $-183°$C. It has accordion-shape absorbers and electrodes. This geometry avoids cracks in the $\phi-$ direction. Over the pseudo-rapidity matched to the inner detector the ECAL has three active layers. These layers are called strips, middle and back. The layer closest to the interaction point (IP), strips, has a very fine granularity, $\Delta\eta \times \Delta\phi = 0.003 \times 0.1$ which makes it possible to distinguish between overlapping showers and allows very precise position measurements of incident particles. The middle layer is deepest in terms of radiation lengths and contains around 80% of the energy of an electromagnetic shower. The cell size is $\Delta\eta \times \Delta\phi = 0.025 \times 0.025$. The third layer collects only the tail of the electromagnetic shower and is therefore less segmented in η. In the range $0 < |\eta| < 1.8$ the ECAL is complemented with a Presampler to estimate the energy lost in the material before the calorimeter. The ECAL provides pointing of photons by determining the position of the photon cluster in the first and the second layer. For $|\eta| > 2.5$ there are only two active layers in the electromagnetic end-cap calorimeter, but they are still sufficient to satisfy the physics requirements for jet and electron reconstruction and E_{T}^{miss} measurements.

The surrounding HCAL consists of three parts: the tile calorimeter, covering $|\eta| < 1.7$, the liquid-Argon hadronic end-cap calorimeter (HEC), located in $1.5 < |\eta| < 3.2$ and the liquid-Argon forward calorimeter (FCAL), covering $3.1 < |\eta| < 4.9$. The tile calorimeter is subdivided into a central barrel and two extended barrels. It uses steel as the absorber and 500 000 plastic scintillator tiles as the active medium. The 68 cm gaps between the central and extended barrels are instrumented with plastic scintillator sheets. The tile calorimeter is divided into three radial layers with cell sizes of $\Delta\eta \times \Delta\phi = 0.1 \times 0.1$ in the first two layers and $\Delta\eta \times \Delta\phi = 0.2 \times 0.1$ in the last layer. The end-caps of the

[15]The material that produces the particle shower is distinct from the material that measures the deposited energy.

hadronic calorimeter again use the liquid-Argon technology, due to the high radiation doses experienced in the forward regions, and the calorimeters are installed in the same cryostats as the EM end-caps. The HEC consists of four layers in depth while FCAL consists of three.

So-called "pileup" can produce noise in the calorimeters and diminish their performance. Pileup arises from extra interactions that can either be overlaid in the same beam crossing with the primary interaction or occur during beam crossings that are close in time to that of the primary interaction, since the response time of the calorimeter is longer than the interval between crossings.

Muon Spectrometer

The muon spectrometer (MS)[16] forms the outer part of the ATLAS detector and is a tracking system, with a range in radius from 4.25 m to 11 m [7, 21]. The muon chambers are situated within a layer of large air-core toroid magnets producing ≈ 0.5 T magnetic field and the muon momentum measurements are based on the magnetic deflection of their tracks. The MS is designed to detect charged particles of transverse momenta greater that 3 GeV and to measure their momentum in the pseudo-rapidity range $|\eta| < 2.7$. It provides a stand-alone transverse momentum resolution better than 10% for particles with energies up to 1 TeV and excellent charge identification.

Precision detectors are located in three layers (stations) at increasing distance from the collision region. Each station includes multiple closely-packed layers measuring the η-coordinate, the direction in which most of the magnetic field deflection occurs. The curves of the tracks are measured with 80 μm resolution.

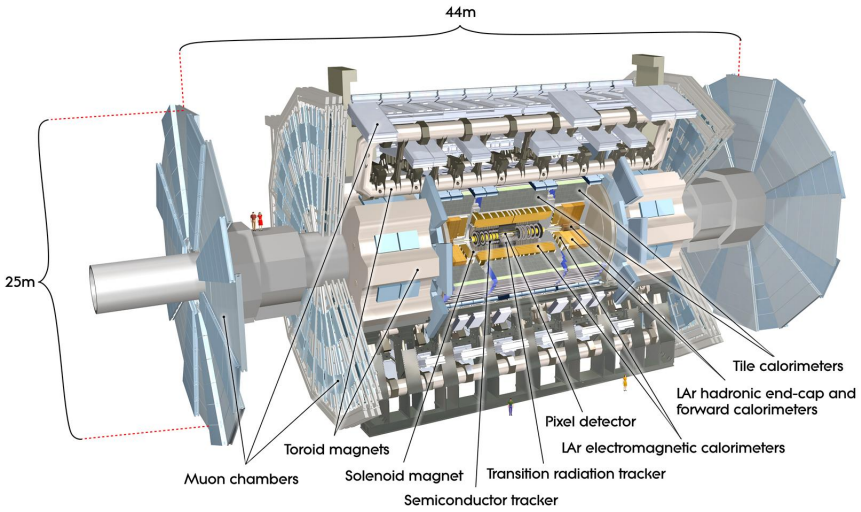

Figure 1.6: Schematic view of the ATLAS detector [22].

1.3.2 Trigger

The number of proton-proton collisions per second is very high, up to 550 million per second (550 MHz) in 2012, while the offline reconstruction capacity is limited to maximal

[16] A spectrometer is an apparatus that is dedicated to measuring momentum.

650 Hz. The data reduction must be handled in such a way that sensitivity for interesting physics processes in not lowered. Three trigger systems handle the data reduction: the Level-1 trigger filters down to ∼75 kHz, the Level-2 trigger filters down to about 2 kHz and the Event Filter does the rest. The Level-1 trigger is a very fast hardware trigger while the others are software [7, 21].

In this analysis both single lepton triggers and dilepton triggers are used. These triggers trigger on leptons containing momentum above a certain value and that have been identified with certain criteria. Half of the single lepton triggers used also require isolation, i.e. that the lepton triggered on is isolated from other particles in the detector.

1.3.3 Event Reconstruction

The recorded data are calibrated, reconstructed, distributed and analysed at over 100 different sites using the World-wide LHC Computing Grid [8]. To begin with, the data selected by the trigger is sent to the CERN Tier-0 computing facility where it is reconstructed. The output is processed and then spread around the world to Tier-1 facilities using the grid. In some cases re-processing is needed, if for example a calibration is updated, and afterwards the data sets are transferred to Tier-2 facilities for further analysis.

In this analysis the final ntuples[17], the so-called D3PDs are used.

1.3.4 Reconstruction and identification of electrons and muons in ATLAS

In many physics processes $e^{\pm}$ and $\mu^{\pm}$ are produced. The energy and momentum of these particles can be well measured and they can be well identified in the detector. However, the rate of QCD jets is much higher at the LHC than the rate of isolated electrons and muons. Hence an excellent particle identification is needed.

When electrons and muons travel through the detector, they interact with the detector material, loosing energy via ionization and radiation. The electrons mainly loose energy via a radiation process called bremsstrahlung[18] in the electromagnetic calorimeter. The dominant absorption process for the photons produced is pair production. Thus the initial electron will lead to a cascade of e^+e^- pairs and photons. Muons rather loose energy via ionization processes, exciting and ionizing atoms along their path. The muon track stays quite narrow throughout the whole detector [49].

Electrons

Electrons are reconstructed using information from both the calorimeter and the inner detector. As the electrons traverse the calorimeter, they deposit their energy in many calorimeter cells. The standard algorithm used to reconstruct isolated high p_{T} electrons in the EM calorimeter is called the "sliding-window" algorithm [11]. The reconstruction is done in two steps. The first step is seed finding and the second step is cluster building. In the seed finding the calorimeter is split up to towers going through the three layers with a cross sectional area $\Delta\eta \times \Delta\phi = 0.025 \times 0.025$ in all layers. These towers are grouped together 5×5 and a local maximum is searched for. If no maximum is found, this group if

[17] Ntuples are files listing all the variables relevant to the events, f.ex. properties of all particles.

[18] The electric field of a nucleus will accelerate and decelerate a passing particle, causing it to radiate photons, and hence loose energy.

moved by one 2nd layer cell and the process repeated until the window contains maximal transverse energy. Then the cluster is built. A group of 3×7 cells [19] is defined around the maxima in the 2nd layer before looking for it in the 1st layer, using the fine 1st layer granularity. Then a maxima is searched for in the third layer and in the presampler. The energy of each electron is calibrated to account for the energy deposited outside the cluster and in dead material. Using a fixed cluster size leads to a very precise calibration. When a cluster with E_{T} above ~ 3 GeV is found in the electromagnetic calorimeter, a matching track is searched for among all reconstructed tracks from the inner detector. The extrapolation of the track back to the electromagnetic calorimeter is required to match the cluster within a broad window of $\Delta\eta \times \Delta\phi = 0.05 \times 0.10$ and the ratio of the energy of the cluster to the momentum of the track is required to be lower than 10. This results in an efficiency of around 93% of reconstructing true electrons with $E_{\mathrm{T}} > 20$ GeV and within the pseudo-rapidity range $|\eta| < 2.5$. The large number of tracks in the inner detector is what decreases the efficiency.

Standard identification of isolated high p_{T} electrons is based on cuts[20] on the calorimeter, tracking and on combined track-cluster variables. Those cuts can all be applied independently. They are a tool to reject background from hadrons faking electrons, non-isolated electrons and electrons from photon conversions. The identification cuts used for physics analysis are labelled loose, medium and tight which reflects how tight they are. A tighter cut has more discriminating variables at each step and tighter requirements on the original variables. In this analysis the tight selection is used. It uses all available particle-identification tools for electron identification [32].

Muons

The most reliable muon reconstruction is achieved when tracks from the muon spectrometer (MS) and tracks from the inner detector (ID) are combined. The muons used for this thesis were reconstructed using the Staco muon combination algorithm [20]. It performs a statistical combination of the track measurements in the MS and the ID. The reconstruction efficiency is about 93%.

1.4 Monte Carlo Event Generation

Monte Carlo (MC) event generators are essential components of almost all experimental analyses. They are also widely used by theorists and experimentalists to make predictions and preparations for future experiments.

The generation process is the following [54]. First it is decided which hard process[21] is wanted. The simulation is started by a pp collision and the probability distribution of the particular hard scattering process is calculated from perturbation theory. Next comes the parton shower phase, where the destiny of incoming and outgoing partons involved in the hard collision, is calculated. Both incoming and outgoing partons in collisions can undergo scattering. Partons carry color charge, and when they are scattered, they radiate gluons. The radiation of incoming particles is called initial state radiation, and the radiation of outgoing particles is called final state radiation. The gluons are coloured

[19] The window is asymmetrical because of the bending of the particle tracks in the ϕ direction caused by the magnetic field in the EM calorimeter.

[20] A cut is a set of selection criteria that defines accepted ranges of several observables.

[21] The hard scatter is the process with highest momentum transfer in the event.

and so an emitted gluon can itself trigger new radiation. Hence extended showers can be produced that fill the phase space with mostly soft gluons. When the momentum scale is low enough, perturbation theory breaks down. Then the generation process is switched to hadronization models. Those models describe the confinement of partons into hadrons, that can be seen in the detector. Usually only one parton of each colliding proton participates in the hard scattering. There is a high probability that the proton remnants interact as well, producing soft hadrons that contaminate the hard process that was already simulated (underlying event), see figure 1.7. Finally, the secondary decay of unstable hadrons is generated. Geant4 [12] is used to simulate the passage of particles through the ATLAS detector. Afterwards the same reconstruction algorithms are used as for the experimental data. The reconstructed objects can be related with the particle level information from the MC. That is, it can be verified, for example, whether a particle reconstructed as an electron really was correctly reconstructed, and also what was the electron's mother particle, the particle that decayed producing the electron. This is called truth matching.

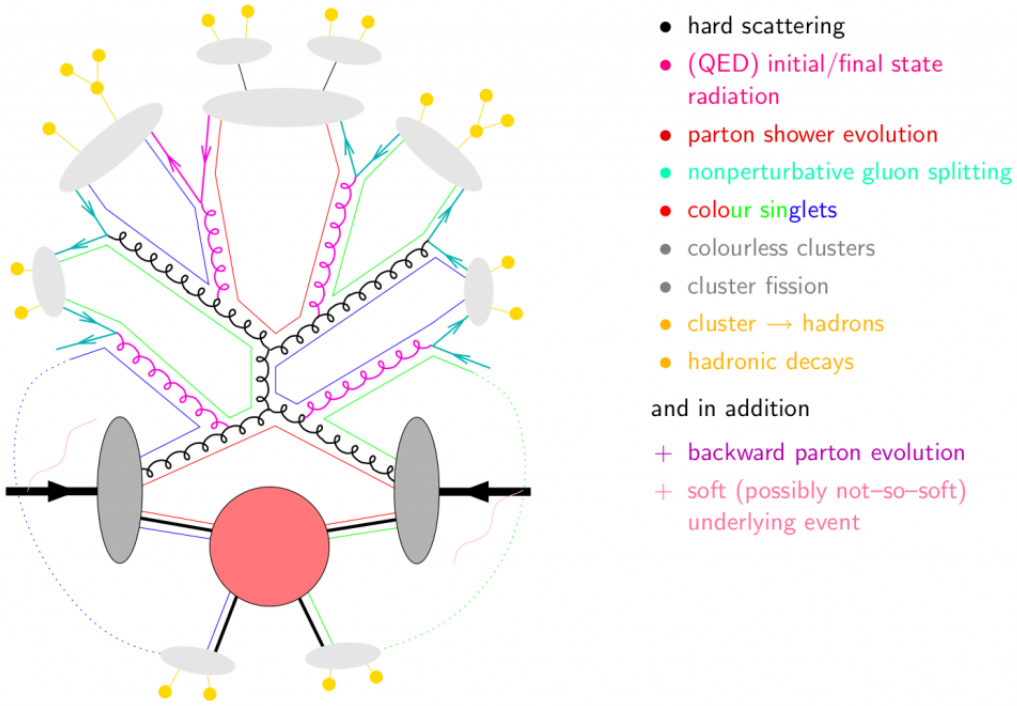

Figure 1.7: Shows the complexity of pp collisions. The two dark gray ellipses are the incoming protons. The big red dot represents the underlying event. The hard-scattering is gluon-gluon scattering, shown in black. Initial and final state radiation is shown in pink. The gluons split into quarks that hadronize. The solid arrowless lines denote color-singlets that form hadrons, light grey ellipses. Those hadrons decay producing jets, clusters of hadrons, many of which decay further [6].

The MC samples used in this thesis are either full simulation or fast simulation samples. Full simulation is the MC generation, for example using Pythia [56], plus the Geant4 simulation of the passage of the generated particles through the detector and the reconstruction of the particles. As the computing time for the Geant4 based detector simulation is significant, a faster (less precise) version was developed. The time-consuming calorimeter part in the Geant4 simulation is sped up by using a parametrisation of the

longitudinal and lateral energy profiles for a shower of a given particle type. The fast simulation is the same as the full simulation in all parts except it uses this fast version of the detector simulation. More information on MC event generation can be found in ref. [54].

1.5 Software

Own C++ code and ROOT framework [16], which is C++ based, are used for the main analysis. Additionally, for the limit setting, the RooStats and RooFit packages [50, 60], that come with ROOT, are used. RooFit is a toolkit for data modelling and fitting. RooStats is built on top of the RooFit package and is used to create advanced statistical tools, like hypothesis testing. Computer facilities at the Experimental High Energy Physics division at Lund University and at CERN are used for computations and the execution time of parallel tasks is reduced by using PROOF [57], which optimally distributes the work over the available resources.

Chapter 2

Prompt same sign dilepton analysis

This chapter describes briefly the main parts of the prompt same-sign dilepton analysis [24]. My contribution to the analysis will be explained in later chapters.

2.1 Event selection

The selection criteria for the analysis changed a bit while I was working on this project and hence those shown here differ slightly from the one used for the official publication. I used the event selection recommended at the time I did my parts of the analysis and the changes made in the selection criteria do not affect my results. The following selection criteria define the so-called signal region, i.e. the region in which a possible signal from new physics would be present.

Events, where it is known that all detectors were working, are selected from the 2012 ATLAS data sample, resulting in a 20.3 fb^{-1} of data. The analysis aims to be inclusive, so same-sign lepton pairs (ee, $e\mu$, and $\mu\mu$) are selected with minimal requirements placed on the non-leptonic activity in the event, such as the number of jets and $E_{\mathrm{T}}^{\mathrm{miss}}$, and a broad p_{T} range is used. Data are collected using dilepton triggers for the $\mu\mu$ channel[1] and the ee channel, i.e. two μ's or two e's must have been triggered on. For the $e\mu$ channel, single lepton triggers are used [27] and I used a single electron trigger for the optimization of the electron isolation cuts.

The reducible SM contributions are suppressed using tight lepton selection criteria, see below. Tau leptons decaying to electrons or muons that pass the identification criteria are considered part of the signal.

2.1.1 Electron selection

The electrons have to fulfil the following criteria (also known as cuts):

- The electron candidate is required to be reconstructed using algorithms for high p_{T} electrons.
- The pseudo-rapidity is required to be $|\eta| < 2.47$, excluding $1.37 < |\eta| < 1.52$. The region is excluded because of a gap between the barrel and end-cap electromagnetic calorimeters where a precise calorimetry is not available.

[1] Channel is a region of the data defined by the corresponding event selection. Channels are required to be mutually exclusive.

- For the highest energetic electron $E_{\mathrm{T}} > 25$ GeV is required and $E_{\mathrm{T}} > 20$ GeV for the second highest.
- Bad quality clusters or fake clusters originating from calorimeter problems are rejected.
- tight++ [32] electron identification is used.
- Prompt electrons[2] are selected by requiring $|d_0|/\sigma(d_0) < 3$. The track impact parameter d_0 is defined as the distance of the track from the interaction vertex projected on the plane perpendicular to the beam axis (the distance of closest approach to the beam axis).
- Also to reject non-prompt electrons it is required that $|z_0 \sin(\theta)| < 1$ mm, where z_0 is the track impact parameter along the beam axis with respect to the interaction point.
- An isolated electron track in the inner detector is selected by requiring the sum of the p_{T} of all tracks inside a cone of radius $\Delta R = \sqrt{\Delta\eta^2 + \Delta\phi^2} = 0.3$ centered around the electron track, excluding the electron track itself, divided by the electron's E_{T} to be less than 0.1 ($p_T^{\mathrm{iso}}(\Delta R = 0.3)/E_{\mathrm{T}} < 0.1$).
- Non-isolated electrons in the calorimeter are rejected by requiring the sum of the E_{T} in a η-ϕ cone of radius $\Delta R = 0.2$ around the direction of the electron in the calorimeter to be less than 3 GeV plus a multiple of its energy: $E_T^{\mathrm{iso}}(\Delta R = 0.2) <$ 3 GeV + $(E_{\mathrm{T}} - 20$ GeV$) \times 0.037$. The energy within the isolation cone is corrected for the leakage of energy from the electron cone core into the isolation cone and for pileup.
- The minimal separation allowed between an electron and a jet is $\Delta R(e, jet) = \sqrt{(\phi_{\mathrm{jet}} - \phi_e)^2 + (\eta_{\mathrm{jet}} - \eta_e)^2} > 0.40$ for jets with $|\eta| < 2.8$, $p_{\mathrm{T}} > 25 + p_{\mathrm{T}}(e) \times 0.05$ GeV, |JVF[3]|> 0.5 if $p_{\mathrm{T}} < 50$ GeV

2.1.2 Muon selection

The muons have to fulfil the following criteria:

- All μ's are reconstructed using information from both the inner detector and the muon spectrometer.
- The so-called staco algorithm [20] is used to reconstruct the muons.
- The pseudorapidity is required to be $|\eta| < 2.5$
- For the highest energetic muon $p_{\mathrm{T}} > 25$ GeV is required and $p_{\mathrm{T}} > 20$ GeV for the second highest.
- The inner detector track must fulfil the following hit requirements [1]:

[2]Electrons created in the beam pipe just after the collision.

[3]The Jet Vertex Fraction (JVF) measures the probability that a jet originated from a particular vertex.

- a b-layer hit is required if the muon traverses an active pixel b-layer module[4].
- the number of hits in the pixel detector plus the number of non-functioning sensors crossed is required to be greater than zero.
- the number of hits in the semiconductor tracker (SCT) plus the number of non-functioning sensors crossed is required to be greater than four.
- the sum of pixel and SCT not fully functioning parts is required to be less than three.
- a successful track extrapolation is required in the acceptance of the TRT.

- Prompt muons are selected by requiring $|d_0| < 0.2$ mm, $|d_0|/\sigma(d_0) < 3$ and $|z_0 \sin\theta| < 1$ mm
- An isolated muon track in the inner detector is selected by requiring the sum of the p_{T} of all tracks inside a cone of radius $\Delta R = \sqrt{\Delta\eta^2 + \Delta\phi^2} = 0.3$ centered around the muon track, excluding the muon track itself, divided by the muon's p_{T} to be less than 0.07 ($p_T^{\mathrm{iso}}(\Delta R = 0.3)/p_{\mathrm{T}} < 0.07$).
- Non-isolated muon tracks in the calorimeters are rejected by requiring the E_{T} within a η-ϕ cone of radius 0.3 around the muon track to be less than 3.5 GeV plus a multiple of its energy: $E_T^{\mathrm{iso}}(\Delta R = 0.3) < 3.5$ GeV $+ (p_{\mathrm{T}} - 20$ GeV$) \times 0.06$. The energy within the isolation cone is corrected for pileup effects.
- The minimal separation allowed between a muon and a jet is $\Delta R(\mu, jet) > 0.40$ for jets with $|\eta| < 2.8$, $p_{\mathrm{T}} > 25 + p_{\mathrm{T}}(\mu) \times 0.05$ GeV, |JVF|> 0.5 if $p_{\mathrm{T}} < 50$ GeV.

Part of my work was to re-evaluate the isolation criteria for electrons and muons. The procedure and results are discussed in chapter 3.

Lepton pairs used are required to come from events where the primary vertex[5] has three or more tracks. They are required to have an invariant mass $m(l^{\pm}l^{\pm}) > 15$ GeV to reduce backgrounds from Drell-Yan processes (see the next section) and low-mass hadronic resonances like the J/ψ. In the case of the electron channel, additionally the mass range $70 - 110$ GeV is vetoed due to large backgrounds from opposite-sign electron pairs produced by Z decays where the charge of one lepton is misidentified. Any combination of two leptons is considered, allowing more than one lepton pair per event to be included.

2.2 Backgrounds

When looking for signals of non-Standard Model processes it is extremely important to understand very well the background.

Non-prompt leptons that appear as prompt or jets reconstructed as electrons are called "fakes". All background processes where at least one of the leptons is fake are called the fake background. Electron fakes come primarily from jets and hadrons which decay in flight or jets which are reconstructed as electrons, while muon fakes arise primarily from

[4]The innermost layer of the pixel detector.

[5]A vertex is an interaction point. A primary vertex in the point of the primary interaction, i.e. the collision point. Hence it is the vertex of that event with the highest $\sqrt{\sum p_{\mathrm{T}}^2}$ value.

b- and c-jets, pions and kaons which decay in flight. A data driven method known as the fake factor method is applied here to evaluate the fake lepton background. I went through the fake factor calculations for the muon channel and I will describe the method in the dedicated chapter, chapter 4. The implementation is very similar for electrons and can be seen in ref. [17].

The main SM processes producing prompt same sign leptons are leptonic decays of two weak bosons. The associated production of a vector boson with a $t\bar{t}$ pair can also result in same-sign dileptons. The contribution is estimated using MC samples which are scaled to the data. The MC samples are also reweighted to have the same pileup profile as the data using a reweighting procedure based on the average number of pileup interactions. Trigger, lepton identification and isolation efficiencies in the MC are corrected for. Energy and momentum smearing[6] of electrons and muons is applied.

At low energies Drell-Yan contamination to prompt like-sign dilepton events is high. The Drell-Yan process is an electromagnetic effect in which a quark and an antiquark from a pair of interacting hadrons annihilate creating a virtual photon or a Z boson, which then decays into an oppositely charged lepton pair.

2.2.1 Charge misidentification

It is important to measure correctly the charge of the leptons. If the charge of one of the leptons is mismeasured, opposite-sign processes contaminate the signal. This charge mismeasurement is usually called charge flip. It is negligible in the muon channel but not in the electron channel, since hard bremsstrahlung events are a common cause of misreconstructed electrons. In those events the produced bremsstrahlung photon converts into an e^+e^- pair and the hardest electron track is oppositely charged compared to the original electron.

The two-lepton invariant mass area around the Z-peak, which is rich in opposite sign leptons, is used to estimate the so-called charge flip rate as a function of η and p_{T}. The charge flip found contributes to the systematic uncertainty.

2.3 Control regions

To gain confidence in the final results, SM predictions are tested in several control regions. Control regions are regions very similar to the signal region but with some of the selection cuts inverted, making them mutually exclusive from the signal region and background enriched.

The opposite-sign control regions are defined using exactly the same event selection as for the like-sign signal region except for the charge requirement. They are mostly used for Monte Carlo corrections. Fake-enhanced control regions are used to test the fake background estimates. They are created by relaxing and reversing impact parameter cuts for muons, relaxing the lepton identification criteria for electrons and changing the isolation requirements.

[6]The momentum and energy resolution of the Monte Carlo samples is usually better than that of the data samples. Therefore their resolution is smeared out to make it similar to that of the data.

2.4 Systematic uncertainties

Systematic effects can change the signal acceptance and the background estimate. For the signal the systematic uncertainties are caused by uncertainties on lepton identification and trigger efficiency, lepton momentum measurement and by uncertainties on the luminosity. For the background estimation the systematic uncertainties come from uncertainties on the fake backgrounds, charge flip, photons reconstructed as electrons and limited statistics available in the Monte Carlo samples.

The systematics are evaluated by varying some of the selection criteria, thus changing the background a little bit and evaluating the effect it has on the signal. There is enough statistics in most of the control regions, so the variation observed should not be affected significantly by the statistical uncertainty in the measurement.

2.5 Unblinding and limit setting

After the steps in the preceding sections have been performed and it has been verified that the results can be trusted, one can analyse the signal region, called unblinding in ATLAS. This procedure is an ATLAS policy, made to ensure unbiased results. The predicted and observed invariant mass distributions of lepton pairs are studied. Positive and negative lepton pairs are studied together and separately.

If no significant excesses are found limits are set on the fiducial cross-section of new sources of prompt, isolated, same-sign leptons. The limit setting is my responsibility and I will explain how limits are done and the statistics behind limit setting in chapter 5. For the final publication the aim is to put also limits on the production cross-section of doubly charged Higgs bosons, but that will not be done by me. When this thesis is handed in, the group has not been allowed to unblind. Hence the limit setting process is not finished.

Chapter 3

Isolation

Due to the higher level of pileup (see section 1.3.1) in the 2012 data compared with the 2011 data, the isolation criteria used in the 2011 analysis [24] are re-evaluated with the tag and probe method using leptonic decays of Z bosons. The tag and probe method is a technique typically used to calculate efficiencies. An unbiased sample of "probe" leptons is selected from the $Z \to ll$ decays by applying the tight analysis selection criteria (see section 2.1) on the other lepton ("tag"). The invariant mass of the pair must lie around the Z boson mass, i.e. 80 GeV $< m_{\text{inv}} <$ 100 GeV, and opposite charge of the leptons is required. Truth matching (see section 1.4) is applied to the MC samples. The tracks of the tag electrons and tag muons in the inner detector (ID) are also required to be isolated to get a cleaner sample. By analysing the probe leptons of all possible lepton pairs in an event I can find the efficiency of the signal passing different isolation cuts and the corresponding background rejection. The signal efficiency is the number of probe leptons passing the isolation cuts divided by the total number of probes. To estimate the background rejection, the selection criteria were changed a bit to select background events. The rejection is then defined as one minus the signal efficiency of these probes.

The optimization done is listed separately for electrons and muons below.

3.1 Electron isolation

It is evaluated whether the cuts used in the previous analysis based on 2011 data are still the optimal ones for this analysis. In the ID the sum of the p_{T} of all tracks inside a $\eta - \phi$ cone of radius $\Delta R = \sqrt{\Delta\phi^2 + \Delta\eta^2} = 0.3$ centered around the electron track, excluding the electron track itself, $p_{\text{T}}^{\text{iso}}(\Delta R = 0.3)$, divided by the electron's E_{T} was required to be less than 0.1 (or $p_{\text{T}}^{\text{iso}}(\Delta R = 0.3)/E_{\text{T}} < 0.1$). The electrons were considered isolated in the calorimeter if $E_{\text{T}}^{\text{iso}}(\Delta R = 0.2) - (E_{\text{T}} - 20 \text{ GeV}) \times 0.037 < 3$ GeV, where $E_{\text{T}}^{\text{iso}}(\Delta R = 0.2)$ is the sum of the E_{T} in a cone of radius $\Delta R = 0.2$ around the direction of the electron in the calorimeter.

The same event and electron selection is used as in the main analysis with a few exceptions. The tag electrons are reconstructed using the tight identification selection as in the main analysis, while the probe electrons are reconstructed using a bit looser criteria, the so-called medium identification criteria [32]. No isolation is applied in the selection of the probes. The data sample used contains 10,071,346 events and the $Z \to ee$ MC, which is a full simulation sample (see section 1.4) generated by Pythia [56], contains 3,587,160 events.

The background is defined as the probes that either fail the medium electron identification selection but pass the loose identification selection, or those that fail the d_0 significance cut. In both cases the probes are required to pass the rest of the electron selection criteria (see section 2.1). There is no invariant mass cut on the background probes, and when using MC samples, the probes are required to fail truth matching, i.e. not being isolated electrons coming from a Z boson decay.

Cuts on both the isolation of the electron in the inner detector and in the calorimeter show better background rejections for similar signal efficiencies than applying a single tight cut on either the isolation in the ID or in the ECAL, as can be seen in figure 3.1. The smallest cone radius, $\Delta R = 0.2$, is used in the calorimeter to minimize the impact of pileup. As this is an inclusive search and not optimized for a specific E_{T} range, it is optimal to use a cut on the isolation of the electron in the calorimeter that relaxes with E_{T}. Thus more background is rejected at lower E_{T}'s, where the signal to background ratio is worse, while at higher E_{T}'s a high electron efficiency is achieved.

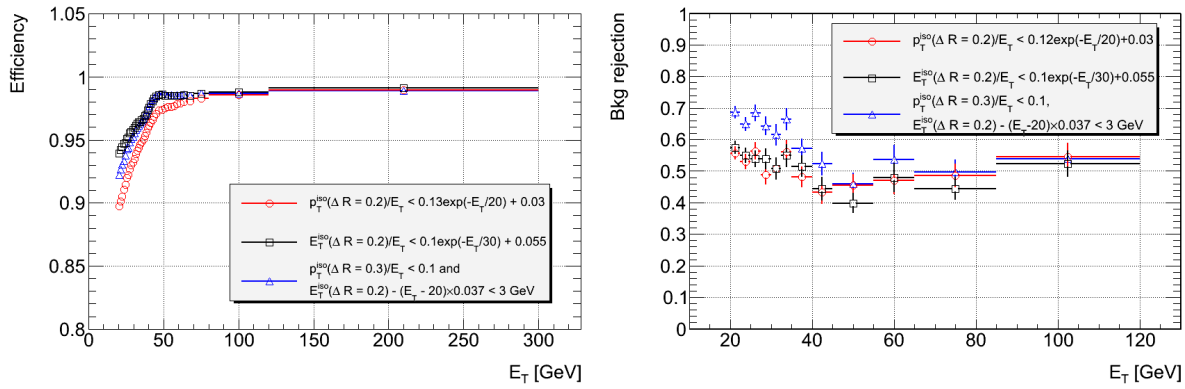

Figure 3.1: Signal efficiency (left) and background rejection (right) as a function of E_{T} of the probe electrons when applying a single cut on the isolation of the electrons in the inner detector (red) or in the calorimeter (black) or if an isolation cut is applied on both (blue). These efficiencies are measured in data.

Due to the high level of pileup in the 2012 data, using a cone size of $\Delta R = 0.4$ in the ID is shown to be less efficient and have worse background rejection than using cone sizes of $\Delta R = 0.2$ and 0.3, which perform similarly well, as shown in figure 3.2. For this analysis a cone size of 0.3 is used for the ID based isolation (or track-based isolation).

The isolation calculations in ATLAS are based on 2 different approaches [48]. The so-called simple-cone isolation draws a cone around the electron cluster in the calorimeter and sums up the E_{T} in all cells within that cone. The topological-cone (topo-cone) isolation also draws a cone around the electron cluster but only sums over the E_{T} in cells that belong to topological clusters, whose centers-of-mass fall into the isolation cone. The topological clusters are built using a seed cell and if the energy of a neighbour cell is significant compared to the noise, it iteratively adds that cell to the cluster. Both methods exclude the electron cone core when summing up the transverse energy within the isolation cone. The isolation computation is illustrated in figure 3.3.

A comparison is done of the performance of these two methods in this analysis. The recommended calorimeter isolation corrections in reference [2] are applied to correct for the pileup effects and the energy leakage from the 5×7 cells electron cone core into the surrounding isolation cone. After the corrections, the topo-cone isolation values,

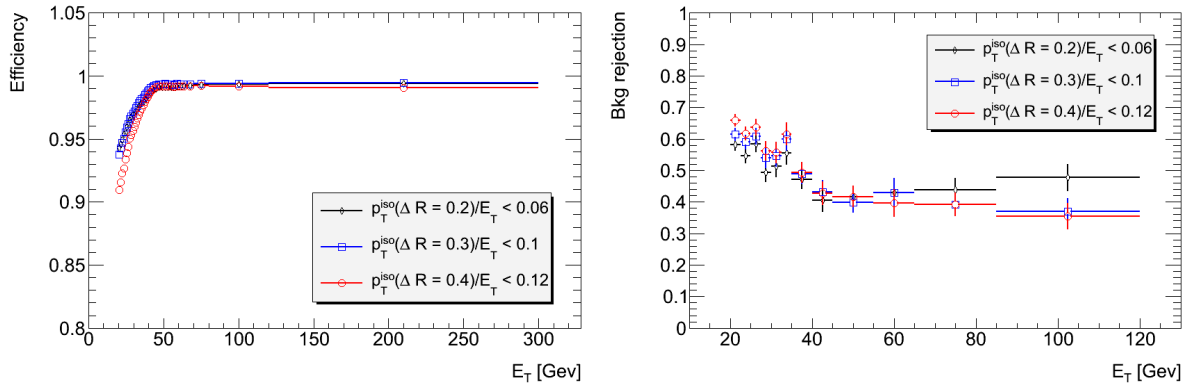

Figure 3.2: Comparison of the signal efficiency (left) and background rejection (right) as a function of E_{T} of the probe electrons, when different cone sizes are used for the isolation cut in the inner detector. The results of using cone size of $\Delta R = 0.2$ are shown in black, $\Delta R = 0.3$ in blue and $\Delta R = 0.4$ in red. Both plots use data.

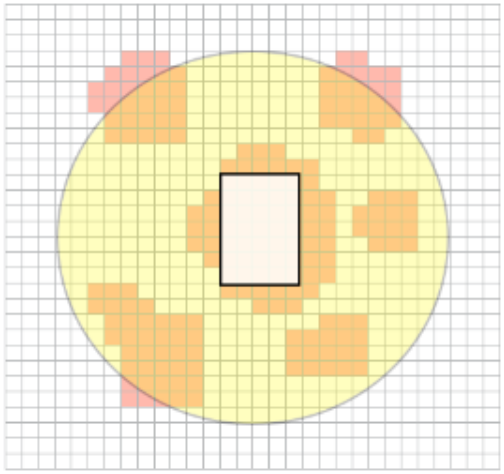

Figure 3.3: Sketch illustrating the isolation computation. The grid represents the granularity in the second layer of the EM calorimeter. The central rectangle (white) contains most of the electron energy. A cone of size $\Delta R = 0.4$ is drawn around the electron cluster (yellow). The simple-cone method uses all cells within the cone, whereas the topological method uses only the cells belonging to the topological clusters with barycenters within the cone (orange). The plot is obtained from ref. [48].

topo-$E_{\mathrm{T}}^{\mathrm{iso}}/E_{\mathrm{T}}$, are independent of pileup, while the simple-cone isolation values, $E_{\mathrm{T}}^{\mathrm{iso}}/E_{\mathrm{T}}$, decrease with pileup, see figure 3.4. Data and MC agree better using the topological algorithm, and in addition, the topo-$E_{\mathrm{T}}^{\mathrm{iso}}/E_{\mathrm{T}}$ distribution is narrower compared to the simple cone based isolation, see figure 3.5. However, a decrease is observed in the signal efficiency with increasing pileup if topological isolation is used (see figure 3.7). As can be seen in figure 3.5, the distributions of the $E_{\mathrm{T}}^{\mathrm{iso}}/E_{\mathrm{T}}$ and topo-$E_{\mathrm{T}}^{\mathrm{iso}}/E_{\mathrm{T}}$ values broaden a bit with pileup. Hence the cause of the efficiency decrease could be that since the topo-cone isolation values are independent of pileup and not decreasing with pileup as the simple-cone values, more leptons could be cut away at high pileup. This was verified by shifting the topo-cone isolation values such that they overlapped with the simple-cone isolation values, after correcting for pileup and energy leakage. A signal efficiency independent of pileup, for both algorithms, was obtained, thus confirming that the broadening of the

topo-$E_{\mathrm{T}}^{\mathrm{iso}}/E_{\mathrm{T}}$ distribution with pileup causes the observed decrease in signal efficiency using topo-cone isolation.

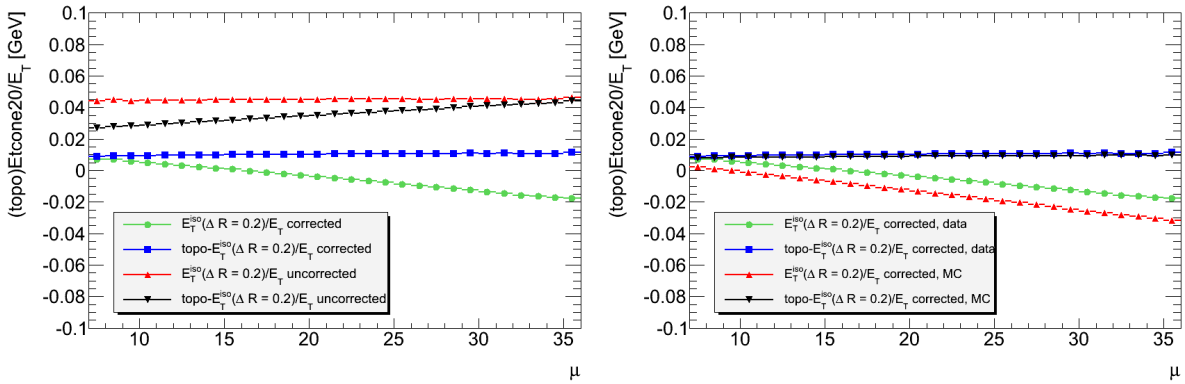

Figure 3.4: Left: Average $E_{\mathrm{T}}^{\mathrm{iso}}/E_{\mathrm{T}}$ and topo-$E_{\mathrm{T}}^{\mathrm{iso}}/E_{\mathrm{T}}$ values before and after calorimeter isolation corrections as a function of pileup, μ. The corrected $E_{\mathrm{T}}^{\mathrm{iso}}/E_{\mathrm{T}}$ values are shown in green, the uncorrected ones are in red. The corrected topo-$E_{\mathrm{T}}^{\mathrm{iso}}/E_{\mathrm{T}}$ values are shown in blue and the uncorrected ones in black. Right: Data and MC comparison after corrections. The $E_{\mathrm{T}}^{\mathrm{iso}}/E_{\mathrm{T}}$ values using data are in green and using MC are in red. The topo-$E_{\mathrm{T}}^{\mathrm{iso}}/E_{\mathrm{T}}$ values using data are in blue and using MC are in black. A cone size of $\Delta R = 0.2$ is used. The MC is a full simulation sample from the 2012 production.

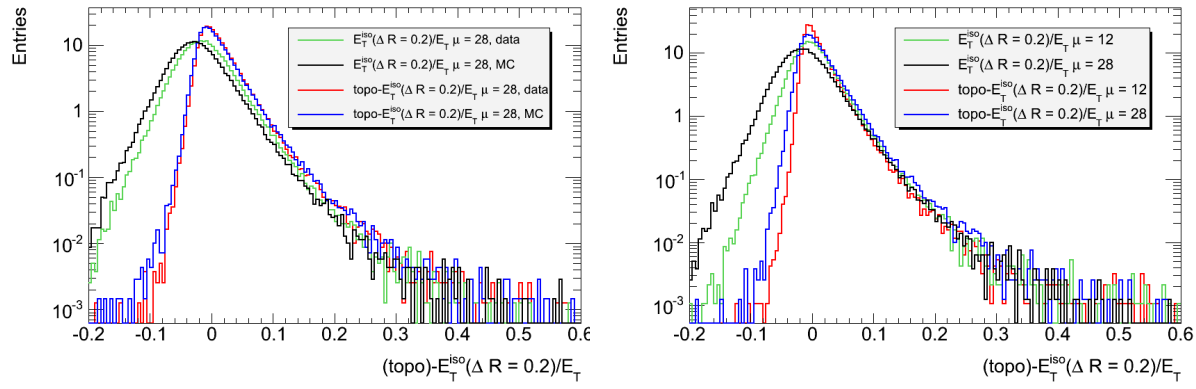

Figure 3.5: Left: Histograms of the isolation values, $E_{\mathrm{T}}^{\mathrm{iso}}/E_{\mathrm{T}}$ and topo-$E_{\mathrm{T}}^{\mathrm{iso}}/E_{\mathrm{T}}$, using a cone size of $\Delta R = 0.2$ for data and MC (full simulation) in events with 28 interactions. The $E_{\mathrm{T}}^{\mathrm{iso}}/E_{\mathrm{T}}$ values measured in data are shown in green and measured in MC in black. The values of topo-$E_{\mathrm{T}}^{\mathrm{iso}}/E_{\mathrm{T}}$ measured in data are displayed in red and measured in MC are blue. Right: The difference in isolation values between beam crossings with 12 and 28 interactions for both isolation methods measured in data using a cone size of $\Delta R = 0.2$. The case when the simple-cone method is used and pileup is $\mu = 12$ is shown in green and in black when $\mu = 28$. When the topo-cone method is used and $\mu = 12$ is shown in red and in blue when $\mu = 28$.

Cuts using different isolation methods, cone sizes and different kinds of E_{T} dependent cuts, a tighter cut on the isolation in the inner detector and a looser one in the calorimeter and vice versa, were studied, but none showed significantly better results than the current cut and hence it was decided to continue using this cut in the 2012 same-sign

dilepton analysis. The isolation cut uses the simple-cone isolation method since it provides constant signal efficiency with respect to pileup. Figure 3.6 presents a comparison of the signal efficiency (left) and the background rejection (right) between data and MC for the chosen isolation cut as a function of E_{T}. Figure 3.7 exhibits the signal efficiency of passing the isolation cut versus pileup using both isolation methods, in data and MC (left) and shows the efficiency as a function of η of passing the isolation cut in data and MC (right).

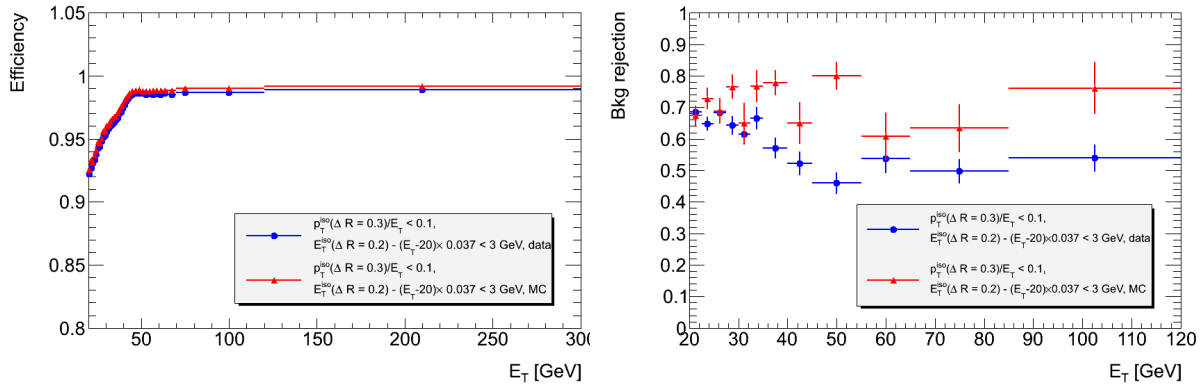

Figure 3.6: Efficiency as a function of E_{T} of the probe electrons passing the isolation cut (left) and the background rejection (right) measured in data and MC (full simulation). The blue points represent the data and the red points represent the MC.

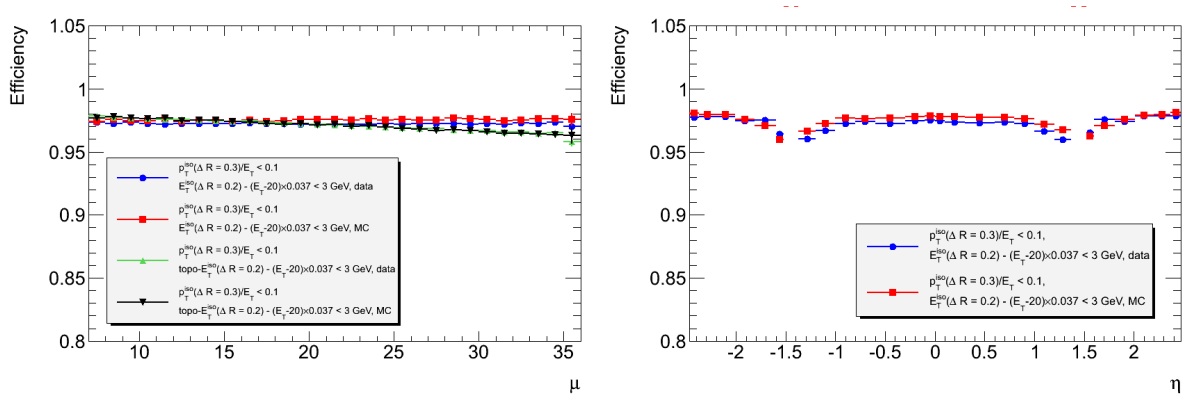

Figure 3.7: Efficiency as a function of pileup (left) and versus η (right) in data and MC (full simulation). The efficiency of passing the chosen isolation cuts measured in data is shown in blue, measured in MC in red. Efficiency passing the same cut, except using a topological cone, measured in data is shown in green, and measured in MC is shown in black.

To investigate the behaviour of the isolation cut at very high E_{T} electrons from $Z \to ee$, Z' and doubly charged Higgs (DCH)[1], MC samples are used. These samples are necessary to have good statistics in all bins in the range from 100 GeV to 1000 GeV. The lowest bin has mainly contributions from $Z \to ee$ and DCH, then the DCH electrons dominate till around 400 GeV and finally the Z' electrons dominate from $\sim$ 650 GeV. The efficiency of passing the isolation cut in this p_{T} range can be seen in figure 3.8.

[1] Z' and DCH are hypothetical new bosons.

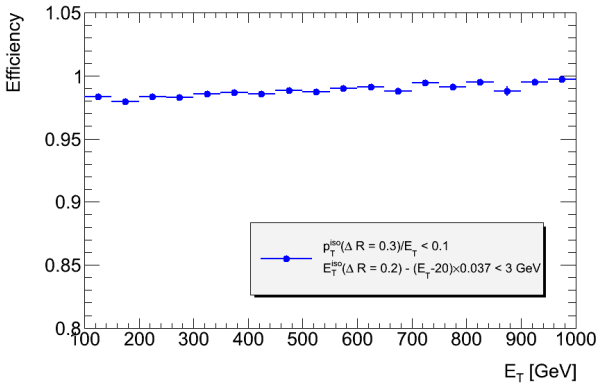

Figure 3.8: Efficiency of passing the isolation cuts measured in Z', DCH and Z MC samples. The $Z \to ee$ and Z' MC's are full simulation samples, while the DCH MC's are fast simulation samples.

3.2 Muon isolation

To optimize the muon isolation criteria, muons from Z decays are used as the signal muons, but because of low background, muons from $c\bar{c}$ and $b\bar{b}$ decays are used to evaluate the background rejection. The data sample used contains 14,341,617 events and the $Z \to \mu\mu$ MC contains 3,856,617 events. The $c\bar{c}/b\bar{b}$ sample contains 1,753,439 events. Both MC samples are based on full simulations using the 2012 production.

It is evaluated whether the cut used in the previous analysis using 2011 data, is still the optimal one for this analysis. In the 2011 analysis only the isolation of the muon track in the ID, $p_{\mathrm{T}}^{\mathrm{iso}}(\Delta R = 0.4)/p_{\mathrm{T}} < 0.06$ and $p_{\mathrm{T}}^{\mathrm{iso}}(\Delta R = 0.4) < (4 + 0.02 \times p_{\mathrm{T}})$ was used, where $p_{\mathrm{T}}^{\mathrm{iso}}(\Delta R = 0.4)$ is the sum of the p_{T} of all tracks inside a cone of radius $\Delta R = \sqrt{\Delta\phi^2 + \Delta\eta^2} = 0.4$ around the muon track, excluding the track itself. The tag and probe method is used, as for the electrons. Additionally to the selection cuts of the probe muons, the tag muons have to fulfil a track-based isolation cut and be triggered on. Since the tag and probes from the $c\bar{c}/b\bar{b}$ sample are by definition background, the same selection criteria are used as for the signal tags and probes, except they are required to not come from a Z boson decay.

A new cut was found, which has a better signal efficiency and a similar or higher background rejection. The muon is considered isolated in the ID if $p_{\mathrm{T}}^{\mathrm{iso}}/p_{\mathrm{T}} < 0.07$ and isolated in the calorimeters if $E_{\mathrm{T}}^{\mathrm{iso}} - (p_{\mathrm{T}} - 20\ \mathrm{GeV}) \times 0.06 < 3.5\ \mathrm{GeV}$. A calorimeter-based isolation cut is applied in addition to a track-based one since it shows a better background rejection for the same signal efficiency than when a single tight track-based or calorimeter-based cut is applied, see figure 3.9. Pileup effects in the calorimeters are corrected for using the recommendations in reference [3]. No increase in pileup dependence is observed, although a calorimeter-based cut is added, as can be seen in figure 3.10. A cone size of $\Delta R = 0.3$ is used for both the track-based and the calorimeter-based cut, since it results in a good background rejection compared to cuts of similar signal efficiencies using other cone sizes, see figure 3.11.

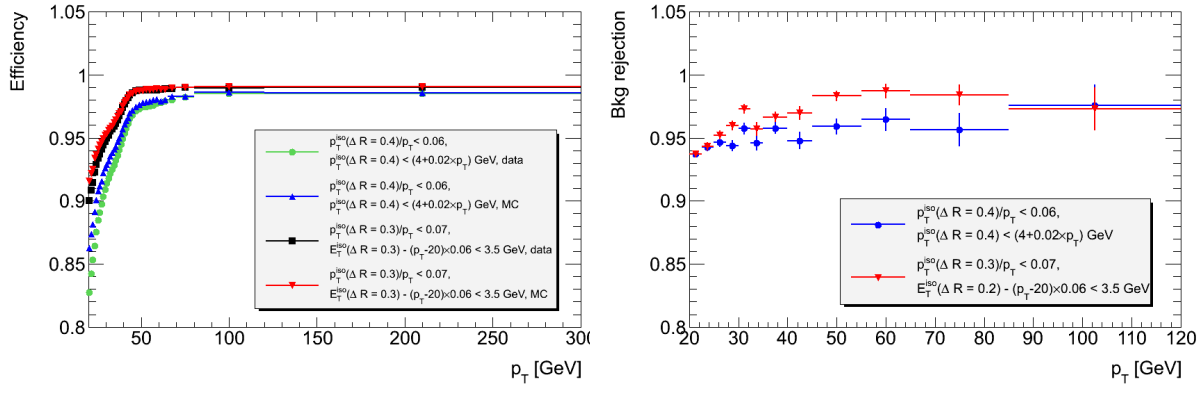

Figure 3.9: Efficiency of the probes passing the old and the new isolation cuts measured in data and MC (left) and background rejections using $c\bar{c}/b\bar{b}$ MC samples (right) as a function of p_T. The old cut is shown in green (data) and in blue (MC). The new cut is shown in black (data) in red (MC). The MC is a full simulation sample.

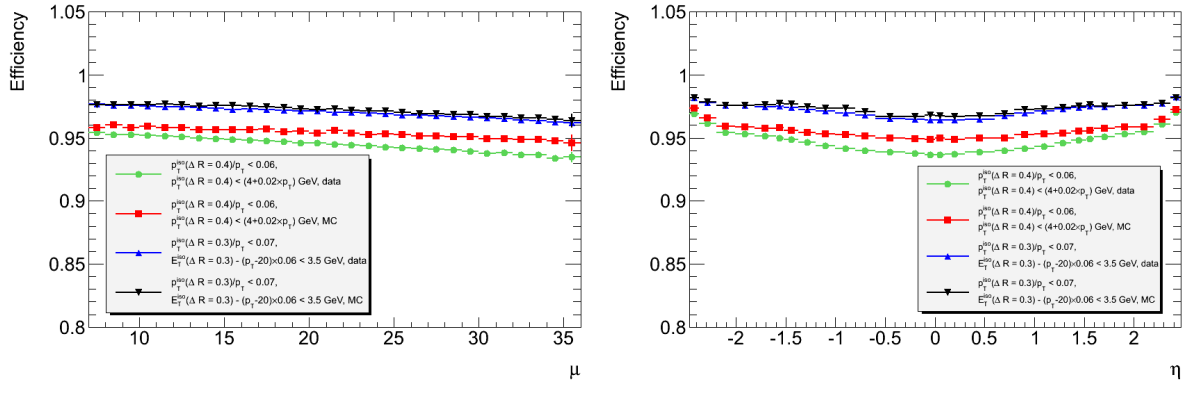

Figure 3.10: Efficiency of the probe muons passing the old and new isolation cuts versus pileup (left) and versus η (right) in data and MC (full simulation). The old cut is displayed in green (data) and in red (MC). The new cut shown in blue (data) and in black (MC).

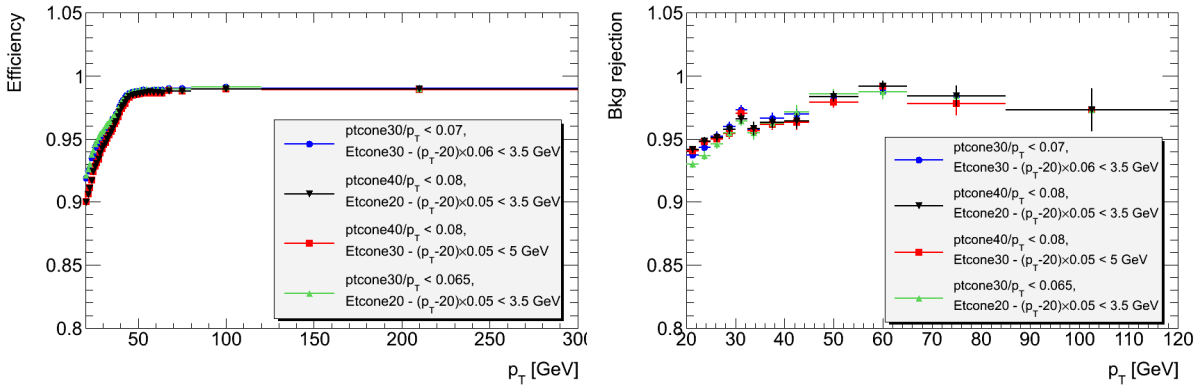

Figure 3.11: Efficiency as a function of p_{T} of the probes passing various track- and calorimeter-based isolation cuts using different cone sizes measured in $Z \to \mu\mu$ MC (left) and background rejections versus p_{T} of the cuts using $\mathrm{c\bar{c}}/\mathrm{b\bar{b}}$ MC samples (right). The cut shown in blue utilizes $\Delta R = 0.3$ in both detectors, and the one shown in red used $\Delta R = 0.4$ (ID) and $\Delta R = 0.3$ (calorimeters). The cut shown in green utilizes $\Delta R = 0.3$ (ID) and $\Delta R = 0.2$ (calorimeters) and cut shown in black uses $\Delta R = 0.4$ (ID) and $\Delta R = 0.2$ (calorimeters). The MC is a full simulation sample.

The same MC samples are used as for the electron channel to investigate the high p_{T} behaviour of the muon isolation cuts as in the case of electrons, except now the bosons are decaying to muons. The result can be seen in figure 3.12. The lowest bin has mainly contributions from $Z \to \mu\mu$ and DCH, then the DCH muons dominate till ∼350 GeV and finally the Z' muons dominate from ∼650 GeV.

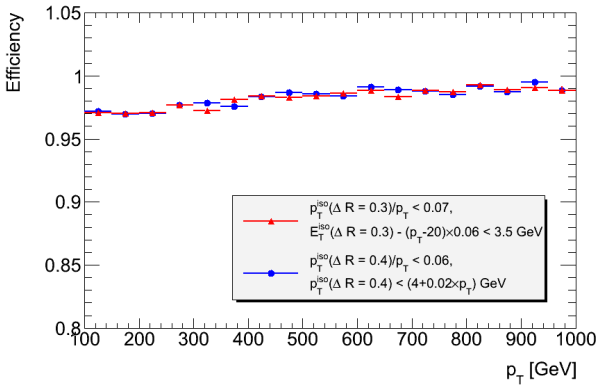

Figure 3.12: Efficiency of passing the old and new isolation cut versus p_{T} measured in Z', DCH and Z MC samples. The efficiency of passing the new cut is shown in red, while passing the old cut is in blue. The $Z \to ee$ and Z' MC's are full simulation samples from the 2012 production while the DCH samples are fast simulation samples.

Chapter 4

Muon fake factor and fake factor systematics

For further comparison of the muon isolation cut used in the previous prompt same-sign dilepton analysis using 2011 data [24], and the new one derived for this analysis (see chapter 3), the so-called fake factor calculations are done for both of them. In the following they will be referred to as the old and the new cut. Both are also referred to as the standard isolation cut.

The fake factor method is a data driven method used to predict the contribution due to fakes[1] in the signal region. The whole 20.3 fb^{-1} of data are used to measure the ratio of leptons passing to failing the standard isolation criteria in a background enriched region (fake factor control region) in various p_{T} and η bins. Failing the isolation cuts means failing either the isolation requirement for the track in the inner detector (ID) or in the calorimeter (ECAL) or in both detectors, but the muons are still required to pass a very loose track-based isolation cut, $p_{\mathrm{T}}^{\mathrm{iso}}(\Delta R = 0.4)/p_{\mathrm{T}} < 1$ where $p_{\mathrm{T}}^{\mathrm{iso}}\Delta R = 0.4$ is the sum of the p_{T} of all tracks inside a $\eta - \phi$ cone of radius $\Delta R = 0.4$ around the muon track in the ID, excluding the muon track itself. Hence in the following all muons that "fail the isolation cuts" still have to pass this loose isolation criterion.

The control region is chosen such that it is similar to the signal region except being poor in prompt leptons and rich in fakes. For the muons this region is taken as the region with reversed d_0 significance cut, $|d_0|/\sigma(d_0) > 3$, and loosened d_0 cut, $|d_0| < 10$ mm, while all the other muon selection criteria are the same as in the main analysis, detailed in section 2.1. Figure 4.1 visualises these regions.

The muons passing the isolation cuts in the fake factor control region are almost all fakes. The ratio of muons passing to failing the isolation cuts in this region can thus be used to test the acceptance of fake muons as prompt by the standard isolation cuts. This ratio is called the fake factor:

$$f = \frac{n_{\mathrm{pass,CR}}}{n_{\mathrm{fail,CR}}} \tag{4.0.1}$$

where $n_{\mathrm{pass,CR}}$ ($n_{\mathrm{fail,CR}}$) is the number of leptons passing (failing) the isolation cuts in the fake factor control region.

Residual contamination of prompt leptons in the control region is subtracted using the MC samples summarized in table 4.1, before computing the fake factor. The samples

[1] Mostly non-prompt muons reconstructed as prompt.

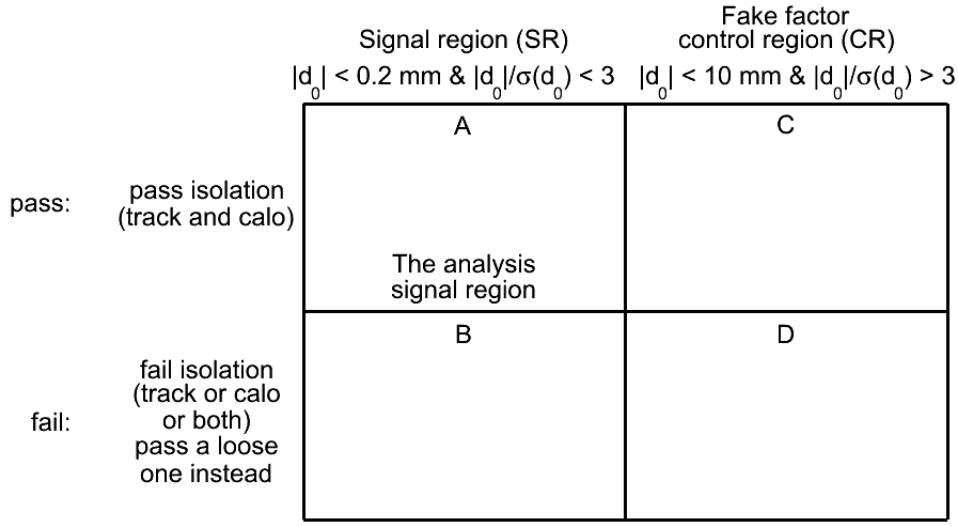

Figure 4.1: The regions used to calculate the muon fake factor and fake factor systematics. Region A is the true signal region used in the analysis. Regions C and D are used to calculate the fake factors. Regions A and B are only used to calculate corrections to the fake factors and the fake factor systematic uncertainties. Region B is a control region but is sometimes referred to as a signal region as it has the same d_0 significance as the true signal region.

are scaled to the data by applying the following sample weight:

$$\text{weight} = \frac{L \times \sigma \times k}{N_{\text{evt}}} \tag{4.0.2}$$

where L is the integrated luminosity, σ is the cross section, k is the k-factor[2] and N_{evt} is the number of events in the MC sample. The cross section, for example, for the process $WZ \to lll\nu$, is the cross section of the colliding protons producing a W and a Z boson which will subsequently decay into three leptons and a neutrino. The samples and their cross section, k-factors, event numbers and weights are listed in table 4.1. Depending on the process different generators are used. For example not all processes are implemented in all generators. This is in particular true for new physics signals. It also can be a given process is implemented using more precise calculations in one generator which is not available in another. Typically we choose the generator best modelling a given process.

The total number of both prompt and all muons passing and failing the standard isolation criteria in the fake factor control region are given in table 4.2, showing that the prompt contamination is negligible. The muons are required to belong to a same-sign muon pair.

The fake factors are found in the fake factor control region while they are applied in the signal region. Since the muon isolation can depend on the impact parameter significance, a correction has to be applied. For this purpose a $b\bar{b}/c\bar{c}$ MC sample is used. The fake factors in both the signal region and in the control region are determined and their ratio, also called a scale factor, is calculated using same-sign muon pairs with $p_{\text{T}} > 10$ GeV and $m(\mu\mu) > 15$ GeV. The whole p_{T} range can be integrated since no p_{T} dependence is observed, as shown in figure 4.2. Table 4.3 presents the MC fake factors and the

[2]A correction factor for unknown or difficult to express effects, often a comparison of σ calculated up to leading order and σ calculated up to next to leading order.

Table 4.1: MC samples producing prompt same sign leptons and their cross section, k-factors, event numbers and weights. The integrated luminosity is 20.3 fb^{-1}.

Process	Generator	Sample no.	σ [pb]	k-factor	N_{evt}	Weight
$W^{\pm}W^{\pm}$	SHERPA [10]	126892	5.503	1.07	2,699,995	0.0443
$W^{\pm}Z$	SHERPA	126893	9.7508	1.06	2,699,893	0.0777
ZZ	SHERPA	126894	8.7345	1.11	3,799,491	0.0518
ZZ	SHERPA	126895	0.49601	1.14	899,899	0.0128
$W^{\pm}W^{\pm}jj$	SHERPA	129800	2.0396	1.0	299,999	0.138
$t\bar{t}$	McAtNlo JIMMY [9, 40]	105200	208.13	1.145	14,990,603	0.32271
$t\bar{t}W^{\pm}$	MADGR. + PYTHIA [15, 56]	119353	0.104	1.0	399,997	$5.28 \cdot 10^{-3}$
$t\bar{t}Z$	MADGR. + PYTHIA	119355	0.067	1.0	399,997	$3.4 \cdot 10^{-3}$

Table 4.2: The number of prompt muons passing and failing the standard isolation criteria in the fake factor control region using the MC samples listed in table 4.1 scaled to the 2012 luminosity and the total number of muons passing and failing those cuts in the fake factor control region, using the complete $\sqrt{s} = 8$ TeV set of data. The muons are required to belong to a same-sign muon pair.

	Monte Carlo		Data	
	n_{pass}, prompt	n_{fail}, prompt	n_{pass}, all	n_{fail}, all
The new cut	29.7	3.1	1639	17389
The old cut	28.8	4.0	1692	17336

corresponding scale factors[3].

Table 4.3: Fake factors for signal and control region muons using both the old and new isolation cuts derived from MC and the corresponding scale factors. The statistical uncertainties shown are calculated using expressions 4.0.4 and 4.0.5.

	Signal region $\lvert d_0\rvert/\sigma(d_0) < 3$, $\lvert d_0\rvert < 0.2$ mm	Control region $\lvert d_0\rvert/\sigma(d_0) > 3$, $\lvert d_0\rvert < 10$ mm	Scale factor
Old cut	0.115 ± 0.009	0.112 ± 0.009	1.02 ± 0.11
New cut	0.141 ± 0.010	0.126 ± 0.010	1.12 ± 0.12

For a result $R = R(x, y, z)$ the statistical uncertainties are:

$$\sigma_R = \sqrt{\left(\frac{\partial R}{\partial x}\right)^2 \sigma_x^2 + \left(\frac{\partial R}{\partial y}\right)^2 \sigma_y^2 + \left(\frac{\partial R}{\partial z}\right)^2 \sigma_z^2} \tag{4.0.3}$$

All statistical uncertainties in this section are calculated according to expression 4.0.3. In the case of the fake factor errors the statistical uncertainty on the number of muons passing and failing is the square root of n_{pass} and n_{fail} respectively so expression 4.0.3 simplifies to

$$\sigma_f = f\sqrt{\frac{1}{n_{\text{pass}}} + \frac{1}{n_{\text{fail}}}} \tag{4.0.4}$$

[3]I used an earlier version of the selection cuts where events containing exactly 2 muons have been preselected. In the more recent analysis this selection has been changed to selecting 2 or more muons.

The error on the scale factor is found using the same formula:

$$\sigma_{SF} = SF\sqrt{\left(\frac{\sigma_{f_{SR}}}{f_{SR}}\right)^2 + \left(\frac{\sigma_{f_{CR}}}{f_{CR}}\right)^2} \tag{4.0.5}$$

where SF is the scale factor, f_{SR} (f_{CR}) is the fake factor in the signal region (control region) and $\sigma_{f_{SR}}$ ($\sigma_{f_{CR}}$) is the statistical uncertainty on the fake factor in the signal region (fake factor control region).

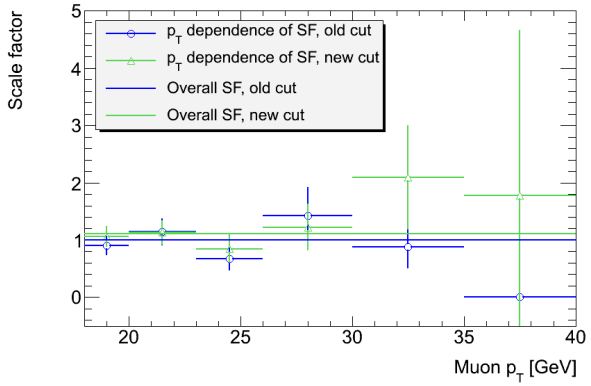

Figure 4.2: p_{T} dependence of the d_0 significance scale factor for the old isolation cut (blue) and the new one (green). The overall scale factors for the old cut and the new cut are also shown in corresponding colors.

When measuring the actual fake factors, the transverse momenta of both muons in a pair are required to be greater than 20 GeV and their invariant mass greater than 15 GeV. The correction factor is applied to the obtained fake factors giving the final fake factors, see figure 4.3. For the new cut the fake factors are shifted upwards by 12% and by 2% for the old cut. The fake factors plotted as a function of η are shown in figure 4.4.

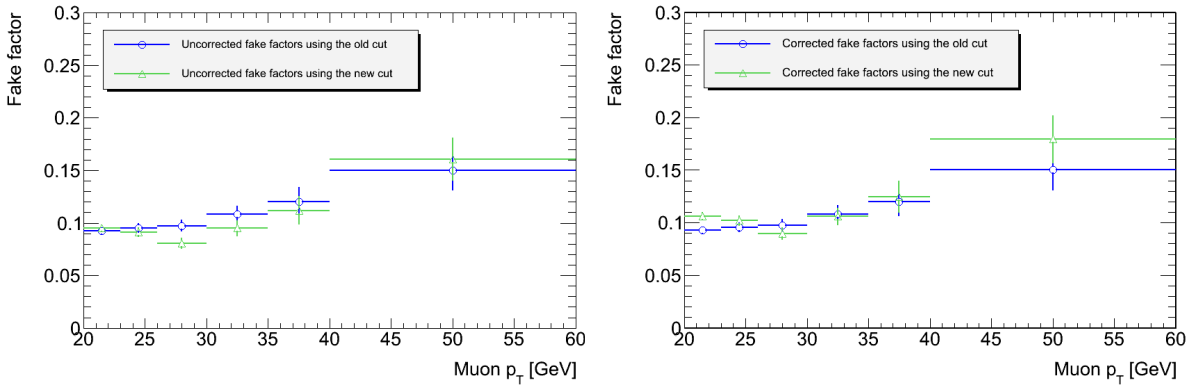

Figure 4.3: Fake factors found using the new and old isolation cuts. Prompt contributions from W/Z+jets and $t\bar{t}$ have been subtracted. The left plot displays the fake factors before correcting for isolation dependence on d_0 significance and the right plot shows the final fake factors after the correction.

The fake factors obtained when the new isolation cut is applied are slightly higher than when using the old cut. A cross check was done (not by myself) to test whether the higher fake factor led to a proportionally higher number of fakes in the signal region.

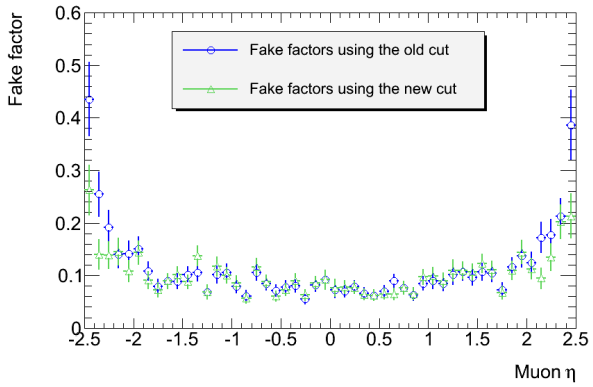

Figure 4.4: The fake factors as a function of η, using the new and old isolation cuts.

The number of prompt muons and fakes in the signal region were measured using the MC samples listed in table 4.1. The result showed that the number of fakes is higher using the new cut, but the number of prompt muons is also substantially higher, resulting in an overall lower percentage of fake to prompt muons passing the new cut (see table 4.4). So, higher fake factors do not have to mean higher percentage of fake muons in the signal region. Information on how to calculate the final fake background prediction can be found in ref. [17].

Table 4.4: The number of prompt and fake muons and ratio of fake to prompt muons passing the old and the new isolation cuts, found using the MC samples utilized for the signal region in table 4.1.

	The old cut	The new cut
Prompt μ's	1106	1219
Fake μ's	185	193
Fake/prompt μ's (%)	14.3	13.7

4.1 Systematic uncertainty associated with the fake factors

Although the fake factor control region is assumed to be similar in kinematics and composition to the signal region, there may be some differences. One such difference is the isolation dependence on the impact parameter significance. The uncertainty on the scale factor is put as a systematic one, resulting in a 12% systematic uncertainty if the new isolation cut is used and a 11% systematic uncertainty if the old cut is used.

Another such difference can be in the number of fake muons coming from heavy flavor decays compared to light flavor decays between the two regions. Light flavor decays are mainly decays of up, down or strange mesons, such as pion and kaon decays, but also up, down or strange baryon decays. Heavy flavor decays are decays of particles containing c or b quarks. The calculation of the fake factor assumes that the non-prompt muons primarily originate from heavy flavor decays but the value of the fake factor if only muons coming from light flavor decays are taken into account can be different. Hence the fake

factor can be biased if the fraction of muons from light flavor decays is different in the signal region than in the fake factor control region.

In this analysis only combined muons are used. These are muons which have been reconstructed by combining the tracks from the muon spectrometer (MS) and the inner detector (ID). The lifetime of light flavor particles is typically longer than the lifetime of heavy flavor particles, therefore light flavor particles usually decay in the detector, while heavy flavor particles decay already in or near the beam pipe. Since the muon is not the only decay product of a light flavor particle, the momentum measured in the MS extrapolated back to the interaction point, correcting for the energy loss in the calorimeters, p^{MX}, is less than the momentum measured in the ID, p^{ID}. The fractional momentum loss between the ID and the MS is defined as

$$\Delta p = (p^{ID} - p^{MX})/p^{ID} \tag{4.1.1}$$

The fractional momentum loss of prompt muons and muons from heavy flavor decays is expected to be symmetric around $\Delta p = 0$, since the mother particle decays before reaching the inner detector. The fluctuation around zero is caused by the limited p_{T} resolution in the ID and the MS.

The fractional momentum-loss asymmetry is defined as

$$\Delta p^{\mathrm{asym}} = \frac{n(\Delta p > 0.1) - n(\Delta p < -0.1)}{n_{\mathrm{tot}}} \tag{4.1.2}$$

where $n(\Delta p > 0.1)$ ($n(\Delta p < -0.1)$) is the number of muons with fractional momentum loss greater than 0.1 (less than -0.1) and n_{tot} is the total number of muons.

The fractional momentum loss asymmetry is proportional to the fraction of muons coming from light flavor decays, the so-called light flavor fraction (x_{LF}). The factor of proportionality is

$$C = \Delta p^{\mathrm{asym}}/\text{Fraction of muons coming from light flavor decays.} \tag{4.1.3}$$

To be later able to estimate the fraction of muons coming from light flavor decays both in the signal and in the control region, this proportionality factor is determined using the $t\bar{t}$ MC sample listed in table 4.1. Muons with $p_{\mathrm{T}} > 20$ GeV that fail the standard isolation cuts are used to measure the fractional momentum loss asymmetry. The fraction of the muons which comes from light flavor decays is measured by applying truth matching to the muons, i.e. the particle level information from the Monte Carlo is used to verify which of the muons are decay products of light or strange mesons or baryons. The results for the fractional momentum loss asymmetry, light flavor fraction and the proportionality constant are presented in table 4.5.

Table 4.5: The fractional momentum-loss asymmetry, light flavor fraction and the resulting propotionality constant, C, for muons failing the standard isolation cuts but passing a loose track isolation instead, obtained using the $t\bar{t}$ MC sample listed in table 4.1. The statistical errors are calculated according to expression 4.0.3.

	Δp^{asym}	Light-flavor fraction	C
New cut	$1.5 \pm 0.1\%$	$0.43 \pm 0.02\%$	3.5 ± 0.3
Old cut	$1.4 \pm 0.1\%$	$0.29 \pm 0.02\%$	5.0 ± 0.5

The proportionality constant is then applied to data to obtain the fraction of muons coming from light flavor decays. The results are shown in table 4.6.

Table 4.6: The fractional momentum-loss asymmetry and fraction of muons coming from light flavor decays for both the new and the old isolation cuts, in the signal region and the control region, for muons failing those cuts. The complete $\sqrt{s} = 8$ TeV set of data is used to extract these numbers. The errors are calculated according to expression 4.0.3.

	Region	Δp^{asym}	Light-flavor fraction
New cut	SR	$3.3 \pm 0.3\%$	$0.96 \pm 0.12\%$
	CR	$1.4 \pm 0.3\%$	$0.39 \pm 0.09\%$
Old cut	SR	$3.4 \pm 0.3\%$	$0.68 \pm 0.09\%$
	CR	$1.4 \pm 0.3\%$	$0.27 \pm 0.07\%$

I define a new fake factor, f_{HFLF}, which is the addition of the fake factor derived for muons coming from light flavor decays, f_{LF}, scaled by the fraction of muons coming from light flavor decays, x_{LF}, and the fake factor derived for muons coming from heavy flavor decays, f_{HF}, scaled by the fraction of muons coming from heavy flavor decays, $x_{HF} = 1 - x_{LF}$. I.e.

$$f_{HFLF} = f_{HF} \cdot (1 - x_{LF}) + f_{LF} \cdot x_{LF} \tag{4.1.4}$$

Assume $f_{HF} \approx f$, where f is the standard fake factor calculated using relation 4.0.1 and integrated over the whole p_{T} range. $f = 0.094 \pm 0.002$ for the new isolation cut and $f = 0.098 \pm 0.002$ for the old isolation cut. The assumption, $f_{HF} \approx f$, is valid since non-prompt muons primarily originate from heavy flavor decays.

I calculate f_{HFLF} in both the signal and the control region to find out how the difference in the fraction of muons coming from light flavor decays between the regions affects the fake factor. The difference in their values, normalized by the standard fake factor f, gives a systematic uncertainty on the fake factor associated to this difference in light flavor fractions between the regions. To be conservative, in this analysis the 1σ upper value of the fraction of muons coming from light flavor decays in the signal region is used, resulting in the following equation for the systematic uncertainty

$$\frac{(f^{+1\sigma}_{HFLF,SR} \cdot SF)}{(f \cdot SF)} - \frac{f_{HFLF,CR}}{f} = \frac{f^{+1\sigma}_{HFLF,SR} - f_{HFLF,CR}}{f} \tag{4.1.5}$$

where SF is the scale factor used to correct for the d_0 dependence of the fake factors (see table 4.3). Using expression 4.1.4 to express the systematic uncertainty in terms of the light flavor fake factor, the standard fake factor and the fraction of muons coming from light flavor decays, one can get

$$\frac{f^{+1\sigma}_{HFLF,SR} - f_{HFLF,CR}}{f} = \frac{(f_{LF} - f) \cdot (x^{+1\sigma}_{LF,SR} - x_{LF,CR})}{f} \tag{4.1.6}$$

The light flavor fractions and the values of the overall standard fake factor using either the old or the new isolation cut are known, hence it is only left to calculate the light flavor fake factors. They are found using a control sample where one muon in a pair fails the impact parameter significance cut. The fake factor is calculated using the second muon in that pair according to the following formula:

$$f_{LF} = \frac{n_{\text{pass}}(\Delta p > 0.10) - n_{\text{pass}}(\Delta p < -0.10)}{n_{\text{fail}}(\Delta p > 0.10) - n_{\text{fail}}(\Delta p < -0.10)} \tag{4.1.7}$$

where $n_{\text{pass}}(\Delta p > 0.1)$ ($n_{\text{pass}}(\Delta p < -0.1)$) is the number of muons passing the isolation cuts with fractional momentum-loss larger than 0.1 (lower than -0.1). The denominator is the same except for muons failing the standard isolation criteria. The calculations result in $f_{LF} = 0.25 \pm 0.03$ for the new isolation cut and $f_{LF} = 0.31 \pm 0.03$ for the old one.

Hence the systematic uncertainty on the fake factor, related to the difference in the number of muons coming from light flavor decays between the signal region and the fake factor control region, using the new isolation cut, is

$$\begin{aligned} \frac{f^{+1\sigma}_{HFLF,SR} - f_{HFLF,CR}}{f} &= \frac{(0.25 - 0.094) \cdot (0.0096 + 0.0012 - 0.0039)}{0.094} \\ &= \frac{0.16 \cdot 0.0069}{0.094} \\ &= 0.012 \end{aligned} \tag{4.1.8}$$

and using the old isolation cut it is

$$\begin{aligned} \frac{f^{+1\sigma}_{HFLF,SR} - f_{HFLF,CR}}{f} &= \frac{(0.31 - 0.098) \cdot (0.0068 + 0.0009 - 0.0027)}{0.098} \\ &= \frac{0.21 \cdot 0.0050}{0.098} \\ &= 0.011 \end{aligned} \tag{4.1.9}$$

I.e. the systematic uncertainty is around 1% using either isolation cut.[4]

The total fake factor systematic uncertainty using the new (old) isolation cut is thus 12% (11%) due to the d_0 significance dependence and 1% (1%) due to light flavor fraction differences between the signal region and the fake factor control region (see table 4.7). The new cut accepts slightly more fakes, hence higher fake factors, but as shown in table 4.4, it also selects more prompt muons, so in the end there is a lower percentage of fakes in the signal region.

Table 4.7: The systematic uncertainties related to the fake factor using both the new and the old isolation cut. I.e. the uncertainty due to the d_0 significance dependence and the uncertainty related to the difference in the number of muons coming from light-flavor decays compared to heavy-flavor decays between the signal region and the fake factor control region.

	$\sigma_{\lvert d_0\rvert/\sigma(d_0)}$ (%)	σ_{LF} (%)
New cut	12	1
Old cut	11	1

[4]The method used to derive this systematic uncertainty is in principle the same as the one used in reference [27]. x_{LF} has though a different meaning in ref. [27].

Chapter 5

Limit Setting

If no excess of signals above the SM background is found, upper confidence level limits are set on the cross section of non-Standard Model processes. The method used for this analysis is the so-called CL_s method [52]. The limits are calculated using RooStats [50] tools. I will in the following explain the main statistical concepts behind the limit setting calculations, go through the RooStats limit setting tools and show the preliminary results obtained for this analysis. The group of researchers working on dilepton analysis had not been allowed to unblind, i.e. analyse the signal region using the 2012 ATLAS data, when this thesis had to be handed in, so my results for the observed limits use dummy numbers.

5.1 The statistics behind limit setting

There are two main approaches in statistics, the *frequentist* approach and the *Bayesian* approach. Since the frequentist approach is used for the limit setting I will focus on this method [36]. A frequentist only associates probabilities with outcomes of repeatable measurements. So the probability of outcome A is defined as the number of times A is obtained when exactly the same experiment is repeated infinite number of times

$$P(A) = \lim_{n\to\infty} \frac{\text{number of times the outcome is A}}{n} \tag{5.1.1}$$

On the other hand, in Bayesian statistics one uses probability to describe one's degree of belief in a given theory or hypothesis. For example, the statement that there is life on other planets can be associated with a probability, since it is uncertain whether it is true or false,

$$P(\text{We are not alone}) = \text{degree of belief that we are not alone in the universe.} \tag{5.1.2}$$

Conditional probability is the probability that an event, let us call it A, will occur given the knowledge that another event, B, has already occurred. This is written as $P(A|B)$ and defined as (for $P(B) > 0$):

$$P(A|B) = \frac{P(A \cap B)}{P(B)} \tag{5.1.3}$$

where $P(A \cap B)$ is the probability of A and B occurring and $P(B)$ is the probability that B will occur.

5.1.1 Hypothesis tests and the profile likelihood ratio

Hypothesis testing is the use of statistics to determine the probability that the predictions of a given model are in agreement with the observed data. Hypothesis tests can be used to construct confidence intervals because there is a one to one correspondence between them. Actually, a confidence interval is a hypothesis test for each value in the interval.

In statistics, a result is called statistically significant if it is unlikely to have occurred by chance alone, according to a pre-determined threshold probability, the significance level. A commonly used significance level is 0.05. Hypothesis tests are used to determine if the outcome of a study leads to a rejection or acceptance of the hypothesis we want to test for a given level of significance. The hypothesis to test is usually called the null hypothesis, or H_0, and it is accompanied by an alternative hypothesis, or H_1. When limits are set, the null hypothesis is the signal plus background hypothesis, i.e. the hypothesis that new physics is needed to explain the data, and the alternative is the background only model, i.e. the hypothesis that the data can be understood with known SM processes. One defines a test of H_0 by specifying a subset of the data space called the critical region, w, such that the probability to observe the data there satisfies

$$P(\mathbf{x} \in w|H_0) \leq \alpha \tag{5.1.4}$$

where α is the significance level. If the data are observed in w then H_0 is rejected. The probability of rejecting H_0 when it is in fact true (a so-called Type-I error) is equal to the chosen significance level, α. α is also known as the size of the test. The probability of falsely accepting the null hypothesis (a so-called Type-II error) is denoted as β. $1-\beta$ is called the power of the test.

A test statistic is considered a numerical summary of a dataset that reduces the data to one value. It can be used to estimate how probable the result we observe is with respect to the null hypothesis. A p-value is defined as the probability of obtaining a test statistic at least as extreme as that observed assuming that the null hypothesis is true. The smaller the p-value, the stronger the evidence against the null hypothesis and one rejects the null hypothesis when the p-value of H_0 is less than α. Hence the p-value and the test statistic define the critical region.

The probability of observing n same-sign lepton pairs given an expectation value of $E(n) = \mu s + b_{\text{tot}}$, can be written as

$$P(n|\mu) = \frac{(\mu s + b_{\text{tot}})^n}{n!} e^{-(\mu s + b_{\text{tot}})} \tag{5.1.5}$$

where s is the number of signal candidates according to the standard value of the model (i.e. the model with $\mu = 1$), b_{tot} is the total number of background candidates and μ is the signal strength, which is the parameter of interest in this search. $\mu = 0$ corresponds to the background only hypothesis, $\mu = 1$ to the standard hypothesis, $\mu = 2$ to twice the standard hypothesis and so forth.

In this analysis b_{tot} arises from several different physics processes, each accompanied by a systematic uncertainty, and then there is also uncertainty related to the luminosity. These uncertainties have to be taken into account when calculating the probability of observing n prompt same-sign lepton pairs. b_{tot} and these uncertainties are not the parameters of interest in H_0 and H_1, i.e. they are so-called nuisance parameters[1] of the models, and will be commonly denoted by θ_p.

[1] All model parameters that are not the parameter of interest.

The uncertainties are incorporated by finding a best fit, a_p, to each nuisance parameter, and relating 1σ uncertainty to this estimate, i.e. θ_p is assumed to have a Gaussian distribution with mean a_p. Hence the uncertainties are included as Gaussian probability density functions[2] (PDF), $f_p(a_p|\theta_p) = G(a_p|\theta_p, \sigma_p = 1)$.

The complete PDF of the signal plus background model is hence a multiple of a Poisson distribution and Gaussian terms

$$f(n, \boldsymbol{a}|\mu, \boldsymbol{\theta}) = \frac{(\mu s + b_{\text{tot}})^n}{n!} e^{-(\mu s + b_{\text{tot}})} \prod_p f(a_p|\theta_p) \tag{5.1.6}$$

where $\boldsymbol{a}$ is the set of best fits to the nuisance parameters and $\boldsymbol{\theta}$ is the set of nuisance parameters in the model. The multiple is over all parameters associated with systematic uncertainties and the luminosity uncertainty. The PDF of the background-only model is the same except the signal strength, μ, has been put to zero. These PDF's are used to calculate the test statistics for the signal plus background and background only models.

According to the Neyman-Pearson lemma, the most powerful test statistic one can construct, i.e. the one with the lowest β value, for models that are free of nuisance parameters, is the likelihood ratio [36]

$$Q = \frac{L(H_1)}{L(H_0)} \tag{5.1.7}$$

where $L(H_1)$ ($L(H_0)$) is the likelihood function of an alternative (null) hypothesis free of nuisance parameters. A likelihood function is a function of the parameters of a model. Let's assume we have a PDF $f(x|\boldsymbol{\alpha})$ where x is the data and $\boldsymbol{\alpha}$ is the set of model parameters. The value of the PDF is a function of the data given a fixed value of these parameters. The likelihood function is numerically equivalent to the PDF, but is a function of these parameters for a given value of the data, i.e. $L(\boldsymbol{\alpha}|x) = f(x|\boldsymbol{\alpha})$. Hence the likelihood function in this analysis is

$$L(\mu, \boldsymbol{\theta}|n, \boldsymbol{a}) = \frac{(\mu s + b_{\text{tot}})^n}{n!} e^{-(\mu s + b_{\text{tot}})} \prod_p f(a_p|\theta_p) \tag{5.1.8}$$

If there are nuisance parameters involved, the Neyman-Pearson lemma is generally not valid. In this case one can replace the simple likelihood ratio in equation 5.1.7 by the profile likelihood ratio [36, 51], used in this analysis:

$$\lambda(\mu) = \frac{L(\mu, \hat{\hat{\boldsymbol{\theta}}})}{L(\hat{\mu}, \hat{\boldsymbol{\theta}})} \tag{5.1.9}$$

where the conditional maximum likelihood estimate[3] $\hat{\hat{\boldsymbol{\theta}}}$ is the value of $\boldsymbol{\theta}$ that maximizes L for a fixed value of the signal strength. It is therefore a function of μ. $L(\hat{\mu}, \hat{\boldsymbol{\theta}})$, on the other hand, is maximized in an unconstrained way, thus $\hat{\mu}$ and $\hat{\boldsymbol{\theta}}$ are the true maximum likelihood estimators. The profile likelihood ratio is therefore bound between 0 and 1. If the hypothesized signal strength coincides with $\hat{\mu}$, it shows an excellent compatibility between the data and the hypothesis, and the profile likelihood ratio approaches one. If

[2] A probability density function is a function of a continuous random variable, whose integral across an interval gives the probability that the value of the variable lies within the same interval.

[3] The maximum likelihood estimate of a parameter is the best fit to that parameter.

instead the assumed μ is far from $\hat{\mu}$ it shows a high degree of incompatibility between the data and the hypothesis and the ratio approaches zero. The distribution of the profile likelihood ratio becomes independent of the values of the nuisance parameters as the number of events approaches infinity. It is the most frequently used likelihood ratio at the LHC.

5.1.2 Constructing upper limits using the CL_s method

The CL_s method is a modification of the standard frequentist method. A likelihood ratio test statistic, q, is used to distinguish between the signal plus background hypothesis and the background-only hypothesis. The corresponding distributions of the test statistic, $f(q|s+b)$ and $f(q|b)$, are found by generating many pseudo-experiments according to both hypotheses and finding the test statistic for each of them. When upper limits are found, a set of values for the parameter of interest, in this case the signal strength, is chosen, and this process is repeated for each value. The observed test statistic is also found for each value of μ. The test statistic[4] used is $q_\mu = -2\ln\lambda(\mu)$, so a low q value means a good compatibility with the null hypothesis. See figure 5.1.

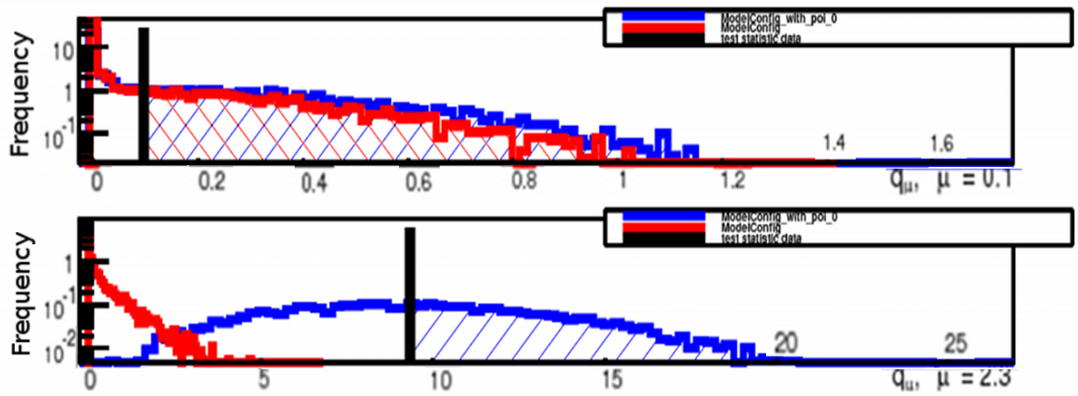

Figure 5.1: The distributions of many profile likelihood ratio test statistics under the signal plus background hypothesis (red) and under the background only hypothesis (blue) obtained using generated pseudo-experiments, and the test statistic obtained from data (black vertical line), for electron pairs with $m_{\text{inv}} > 15$ GeV. The p_{s+b} and $1 - p_b$ values are obtained by integrating over the part of the relevant distribution to the right of the observed test statistic. The upper plot is obtained for a signal strength of ~ 0.1 and the lower one for a signal strength of ~ 2.3. The observed test statistic is obtained using dummy numbers.

Let q_{obs} be the value of the test statistic obtained from the actual data and p_{s+b} and p_b the p-values for the signal plus background model and for the background-only model respectively. They are calculated according to the following equations

$$p_{s+b} = P(q \geq q_{\text{obs}}|s+b) = \int_{q_{\text{obs}}}^{\infty} f(q|s+b)dq \tag{5.1.10}$$

[4]It is asymptotically distributed according to a χ^2_1 function. The degrees of freedom are equal to the difference between the number of maximization parameters in the denominator and the numerator and in this case one parameter is maximized in the numerator and two in the denominator.

and

$$p_b = 1 - P(q \geq q_{\text{obs}}|b) = 1 - \int_{q_{\text{obs}}}^{\infty} f(q|b)dq \tag{5.1.11}$$

Then CL_{s+b} and CL_b are defined as p_{s+b} and $1 - p_b$, respectively.

One could carry out a standard hypothesis test of the $s + b$ hypothesis based on its p-value but thus exclude all hypotheses, with probability close to 5%, independent of the sensitivity to these hypotheses. That does not work in case the expected number of signal events is much less than that of the background, because the distributions of the test statistics under both the background-only and signal plus background hypotheses are overlapping with each other. To avoid excluding signals for which the search is not sensitive to the CL_s method excludes a signal model when

$$CL_s \equiv \frac{CL_{s+b}}{CL_b} < \alpha \tag{5.1.12}$$

For widely separated distributions the $CL_s \approx CL_{s+b}$ but if the overlap increases, CL_b decreases and therefore CL_s increases. This results in the CL_s method being more conservative in excluding signal models than standard frequentist methods when the sensitivity is low.

CL_s values are calculated for a range of μ values and a p-value curve can be produced. An upper limit can be derived by inverting this curve (see figure 5.2). This is called hypothesis inversion. One takes the upper limit to be the largest value of the signal strength which is not excluded. Hence a 95% confidence level (C.L.) upper limit is the signal strength which has a p-value of 0.05. One can see in figure 5.2 that the 95% C.L. upper limit found using the CL_s method is ~ 1.05, while using the CL_{s+b} values it is ~ 0.9. For higher values the $s + b$ model is rejected.

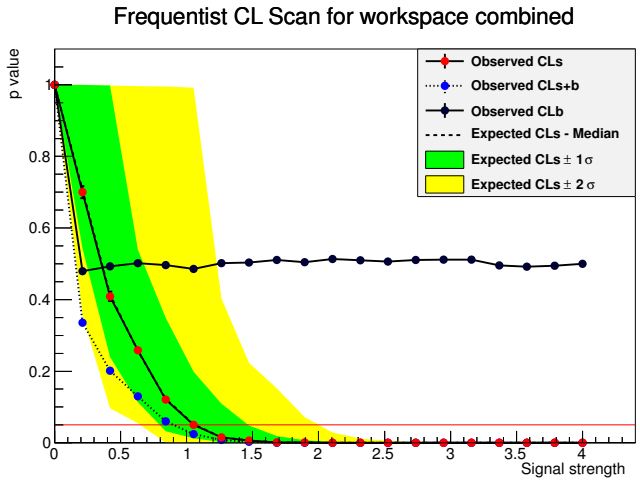

Figure 5.2: p-value curve for same sign electron pairs with $m_{\text{inv}} > 15$ GeV. The red points show the observed CL_s values, the blue points show the observed CL_{s+b} values, and the black points show the CL_b values. The dashed line shows the expected CL_s values (median). The green strip is the expected $CL_s \pm 1\sigma$ and the yellow strip is the expected $CL_s \pm 2\sigma$. The horizontal red line at p-value of 0.05 is the significance of the test, α.

5.2 The limit setting program

In the previous section the statistics behind the limit setting has been explained. In this section I will discuss how they are implemented in the limit setting program used in this analysis.

As input the user has to specify the minimal and maximal value of the signal strength to scan and the number of scans to perform. The user must also specify the number of *toys* to use, i.e. how many pseudo-experiments should be generated when testing the hypotheses. Then the process starts. The expected number of events for each background physics process, the background uncertainties and the luminosity uncertainty are read by `HistFactory` [38]. Based on this information `HistFactory` builds up the full signal plus background PDF. The `RooStats` class `ModelConfig` groups together all the model specifications, like these PDF's, the parameter of interest, the nuisance parameters and the observable, thus defining the null and alternative model. The background-only model is just copied from the signal plus background model, and the signal strength is put to zero.

The hypothesis test calculator class, `FrequentistCalculator`, is created using as input the signal plus background model, the background-only model and the data, i.e. the number of prompt same-sign lepton pairs observed. The number of toys to use is passed to it. The `HypoTestInverter` class is initialized and told to use the `FrequentistCalculator` and the CL_s method, with a confidence level of 95%. Next, the `ToyMCSampler` is configured. `ToyMCSampler` generates a pseudo-experiment for given values of the model parameters and evaluates the test statistic using minimization. The test statistic is set as the profile likelihood and it is put as "one sided", i.e. only positive values allowed.

Now the `GetInterval` function is called and the inverter is run for each value of the signal strength. The scans are performed in a parallel mode using PROOF [57]. In this step the hypothesis tests are performed by `FrequentistCalculator` involving the generation of pseudo-experiments, the test statistics finding and CL_s-value calculations from the p-values of the signal plus background and the background-only hypotheses. By looking at the confidence level curve of the result, an upper limit is derived using an interpolation on the scanned points. The inverter returns a class called `HypoTestInverterResult` containing all the informations about the observed and expected limits.

Two figures are produced to find the suitable number of points and maximal value of the signal strength to scan, and the number of MC toys to use. The first one, see figure 5.2, contains a plot of the observed and expected p values, with 1σ and 2σ error bands on the expected values, as a function of the signal strength. The range in signal strength is large enough if the $CL_s + 2\sigma$ value is well below the significance level, 0.05, before the maximal value of the signal strength is reached for all channels and mass bins. The other figure produced, partly displayed in figure 5.1, contains one plot for each signal strength point. Each plot shows the distributions of the test-statistic, q, for the signal plus background and the background only hypotheses and the test statistic obtained from data. Enough toys are used, i.e. enough experiments are generated, if the generated distributions are relatively smooth.

5.3 Results

For the limit setting one identifies the observables in the experiment on which the search is based. The observable in this analysis is the number of same-sign lepton pairs fulfilling the selection criteria described in chapter 2. Positively charged pairs and negatively charged ones are also studied separately. Let us denote this observable by n. The expectation value of n can be written

$$E(n) = \mu s + b_{\text{tot}} \tag{5.3.1}$$

where μ, s and b_{tot} have the same meaning as before. The output of the limit setting program is the observed and expected upper limit on the signal strength and the 1σ and 2σ error bands on the expected upper limit. But before the limit setting calculations start I choose the number of signal events, s, such that the resulting upper limit on the signal strength is close to one. The upper limits are multiplied with the number of signal events to obtain the observed and expected number of lepton pairs due to non-SM physics in each signal region, $\mu_{\text{obs}}s$ and $\mu_{\text{exp}}s$, respectively. The preliminary results can be seen in tables 5.1, A.1 and A.2. Since this thesis had to be handed in before the number of prompt same-sign lepton pairs was obtained from the data, my results only contain the real expected numbers, dummy numbers are used for the observed ones.

Table 5.1: 95% C.L. upper limit on the number of lepton pairs due to non-SM physics in each lepton channel and mass bin. The 1σ and 2σ bands are given on the expected limit. The observed limits are based on dummy numbers.

	95% C.L. upper limit [number of events]					
	$e^{\pm}e^{\pm}$		$e^{\pm}\mu^{\pm}$		$\mu^{\pm}\mu^{\pm}$	
Mass range	expected	observed	expected	observed	expected	observed
$M > 15$ GeV	$436.10^{+170.88++389.03}_{-107.98--174.00}$	438.04	$827.73^{+255.88++490.11}_{-177.51--313.31}$	826.13	$121.51^{+45.68++98.04}_{-30.23--38.50}$	90.61
$M > 100$ GeV	$235.77^{+85.04++194.45}_{-50.80--110.04}$	233.26	$314.45^{+93.55++193.38}_{-76.90--159.45}$	306.77	$54.66^{+21.78++48.23}_{-12.96--21.89}$	40.86
$M > 200$ GeV	$81.59^{+36.03++73.72}_{-19.28--36.02}$	80.54	$73.64^{+24.25++57.26}_{-17.35--40.57}$	66.52	$21.84^{+10.07++20.68}_{-5.05--9.62}$	17.34
$M > 300$ GeV	$38.34^{+14.56++32.26}_{-9.01--16.08}$	38.07	$30.82^{+11.96++26.81}_{-7.78--12.49}$	27.57	$12.43^{+5.25++10.69}_{-3.31--4.39}$	12.29
$M > 400$ GeV	$21.54^{+7.09++17.03}_{-5.05--8.38}$	21.86	$17.76^{+8.01++17.53}_{-5.20--9.44}$	13.51	$7.38^{+3.04++6.82}_{-1.82--3.16}$	7.18
$M > 500$ GeV	$16.41^{+5.27++10.28}_{-3.47--4.80}$	16.71	$10.62^{+4.72++11.93}_{-2.84--4.32}$	7.80	$4.74^{+2.10++5.03}_{-1.11--1.49}$	4.40

In the previous analysis using 2011 data, the highest mass bin was $m_{\text{inv}} > 400$ GeV. This year we will be able to look at higher masses since we have 4 times higher statistics in the 2012 data compared to 2011 and an increased center-of-mass energy from 7 to 8 TeV.

$1 - CL_b = p_b$ is the probability of obtaining data at least as extreme as that observed, given the background-only hypothesis is true. So, for example, a $1 - CL_b$ value of 0.15 would mean that in 15% of the times a background only pseudo-experiment is repeated, a number of lepton pairs at least as high as the one observed would be obtained. Unfortunately, I do not have these numbers since the signal region has not been analysed yet.

To calculate the cross section of non-SM physics in the fiducial region one must know the efficiency of the selection cuts (see chapter 2), with respect to that region. The efficiency of the selection cuts is defined as the number of pairs that pass the standard selection cuts and the cuts that define the fiducial region divided by those that pass the fiducial cuts. This efficiency is often called the acceptance. It is calculated for a few beyond Standard Model (BSM) models using MC samples and truth matched leptons (see section 1.4). The cuts defining the fiducial region and the list of MC samples used

can be seen in ref. [27] as well as the resulting efficiencies of the selection cuts for the different BSM models.

The fiducial cross-section is defined as

$$\sigma_{95}^{fid}(ll) = \frac{N_{95}}{\epsilon_{fid} L} \tag{5.3.2}$$

where N_{95} is the upper limit on the number of lepton pairs, ϵ_{fid} is the efficiency in the fiducial region and L is the 2012 integrated luminosity. We want to set conservative limits on the upper cross-section and use therefore the lowest observed efficiencies in the fiducial region. The limits in this thesis were set using efficiencies from the 2011 analysis [17] since the updated ones have not yet been calculated. The numbers are 43.4% for the ee channel, 55.2% for the $e\mu$ channel and 59.2% for the $\mu\mu$ channel. The fiducial cross-section limits are shown in tables 5.2, A.3 and A.4 and in figures 5.3, A.1 and A.2.

Table 5.2: 95% C.L. upper limit on the fiducial cross-section of non-SM physics in each lepton channel and mass bin. The 1σ and 2σ bands are given on the expected limit. The observed limits are based on dummy numbers.

	95% C.L. upper limit [fb]					
	$e^{\pm}e^{\pm}$		$e^{\pm}\mu^{\pm}$		$\mu^{\pm}\mu^{\pm}$	
Mass range	expected	observed	expected	observed	expected	observed
$M > 15$ GeV	$49.55^{+19.41++44.20}_{-12.27--19.77}$	49.77	$73.94^{+22.86++43.78}_{-15.86--27.99}$	73.79	$10.12^{+3.80++8.17}_{-2.52--3.21}$	7.55
$M > 100$ GeV	$26.79^{+9.66++22.09}_{-5.77--12.50}$	26.50	$28.09^{+8.36++17.27}_{-6.87--14.24}$	27.40	$4.55^{+1.81++4.02}_{-1.08--1.82}$	3.40
$M > 200$ GeV	$9.27^{+4.09++8.38}_{-2.19--4.09}$	9.15	$6.58^{+2.17++5.12}_{-1.55--3.62}$	5.94	$1.82^{+0.84++1.72}_{-0.42--0.80}$	1.44
$M > 300$ GeV	$4.36^{+1.65++3.67}_{-1.02--1.83}$	4.33	$2.75^{+1.07++2.39}_{-0.69--1.12}$	2.46	$1.04^{+0.44++0.89}_{-0.28--0.37}$	1.02
$M > 400$ GeV	$2.45^{+0.81++1.93}_{-0.57--0.95}$	2.48	$1.59^{+0.72++1.57}_{-0.46--0.84}$	1.21	$0.61^{+0.25++0.57}_{-0.15--0.26}$	0.60
$M > 500$ GeV	$1.86^{+0.60++1.17}_{-0.39--0.55}$	1.90	$0.95^{+0.42++1.07}_{-0.25--0.39}$	0.70	$0.39^{+0.17++0.42}_{-0.09--0.12}$	0.37

As an example, in 95% of the times we would repeat this experiment (hypothetically) we should not observe a higher cross-section for a non-SM production of two same-sign electrons with invariant mass greater than 200 GeV, than 9.27 fb. The dummy number used for the observed limit fits well to the background-only hypothesis in this case.

If the observed limits fit well to the estimated limits, new processes which create two same-sign leptons, with higher cross-sections, can be excluded with 95% probability.

I will extract the limits for the paper once the group is allowed to analyse the data.

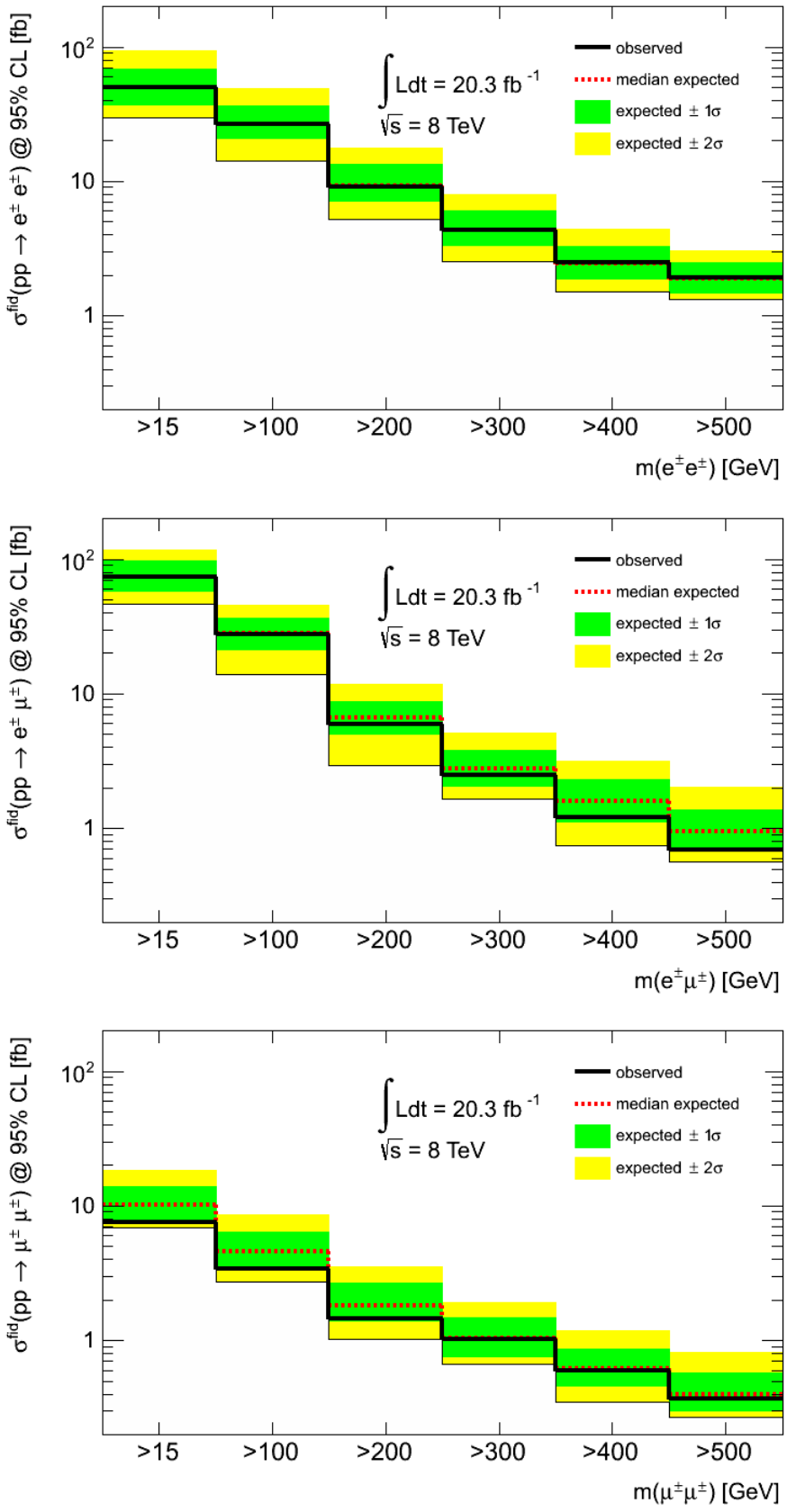

Figure 5.3: 95% C.L. upper limit on the fiducial cross-section of non-SM physics in each lepton channel and mass bin. The 1σ and 2σ bands are given on the expected limit. The observed limits (black solid line) are based on dummy numbers.

Chapter 6

Conclusions

For my thesis I participated in the search for anomalous production of prompt, same-sign lepton pairs, using the ATLAS detector.

I studied the signal efficiencies and background rejections of many different electron and muon isolation cuts, using a Z tag and probe method on both data and Monte Carlo samples. For the electrons I found out that the cut applied in the previous analysis using 2011 data, was still the optimal one for this analysis. However, for the muons I was able to achieve a better signal efficiency for a similar or even better background rejection by adding a cut on the calorimeter isolation, compared to applying only a single cut on the isolation of the track in the inner detector. Both the electron and muon calorimeter-based isolation cuts relax with E_{T}. Thus more background is rejected at low E_{T}, where the signal to background ratio is worse, while a high lepton efficiency is achieved at high E_{T}.

The muon fake factors are calculated in a data-driven way using muon pairs having the same charge. The fake factors obtained using the new muon isolation criteria are slightly higher compared to using the isolation criterion from the previous analysis, but the new cut also accepts substantially more prompt, same-sign muons, resulting in a lower ratio of non-prompt to prompt muons in the signal region. Using either the new or the old isolation cut results in similar systematic uncertainties related to the fake factors, around $11 - 12\%$.

As we are working on publishing a paper on the results of the dilepton search, we were not yet allowed to analyse the signal region according to the ATLAS rules. Hence it is not yet known whether the data agrees with the predictions from known physics processes. If no excess is found in the number of lepton pairs I will put limits on the cross section of new resonances. In the moment I am only allowed to calculate the expected limits but I will extract the observed limits in time. We will be able to look at higher masses in this analysis since we have 4 times higher statistics in the 2012 data compared to 2011 and an increased center-of-mass energy from 7 to 8 TeV.

Bibliography

[1] ATLAS Muon Combined Performance, Guidelines for Analyses of 2012 Data: Criteria for the associated inner detector track (all muon collections). Described at `https://twiki.cern.ch/twiki/bin/viewauth/AtlasProtected/MCPAnalysisGuidelinesData2012#Criteria_for_the_associated_inne`. Only accessible by ATLAS members. Retrieved January 6th, 2014.

[2] Electron Calorimeter Isolation Corrections. Described at `https://twiki.cern.ch/twiki/bin/viewauth/AtlasProtected/CaloIsolationCorrections`. Only accessible by ATLAS members. Retrieved January 6th, 2014.

[3] Muon Calorimeter Corrections. Described at `https://twiki.cern.ch/twiki/bin/viewauth/AtlasProtected/MuonCalorimeterCorrections`. Only accessible by ATLAS members. Retrieved January 6th, 2014.

[4] RooFit RooStats. `http://www.slac.stanford.edu/grp/eg/minos/ROOTSYS/pro/roofit/doc/v530/`. Retrieved January 6th, 2014.

[5] The Injector Chain. Figure from `http://blog.vixra.org/2011/05/29/new-luminosity-record-for-lhc/`. Retrieved January 6th, 2014.

[6] When Feynman Diagrams Fail. `http://www.quantumdiaries.org/2010/12/11/when-feynman-diagrams-fail/`, 2010. Retrieved January 6th, 2014.

[7] ATLAS fact sheets. `http://www.atlas.ch/pdf/ATLAS_fact_sheets.pdf`, 2011. Retrieved January 6th, 2014.

[8] The Worldwide LHC Computing Grid. `http://home.web.cern.ch/about/computing/worldwide-lhc-computing-grid`, 2013. Retrieved January 6th, 2014.

[9] Jimmy. `http://jimmy.hepforge.org/`, Retrieved January 6th, 2014.

[10] Sherpa. `https://sherpa.hepforge.org/trac/wiki`, Retrieved January 6th, 2014.

[11] C. Adam-Bourdarios and S. Snyder et al. EM Calorimeter Calibration and Performance. *CSC-EG-06*, 2008.

[12] S. Agostinelli et al. Geant4—a simulation toolkit. *Nuclear Instruments and Methods in Physics Research Section A: Accelerators, Spectrometers, Detectors and Associated Equipment*, 506(3):250–303, 2003.

[13] A. G. Akeroyd, C.-W. Chiang, and N. Gaur. Leptonic signatures of doubly charged Higgs boson production at the LHC. *JHEP*, 1011(005), 2010. arXiv:1009.2780 [hep-ph].

[14] J. Alwall, P. Schuster, and N. Toro. Simplified Models for a First Characterization of New Physics at the LHC. *Physics Review D*, 79, 2009. arXiv:0810.3921 [hep-ph].

[15] J. Alwall et al. MadGraph. *JHEP*, 1106(128), 2011. arXiv:1106.0522 [hep-ph].

[16] I. Antcheva et al. ROOT — A C++ framework for petabyte data storage, statistical analysis and visualization. *Computer Physics Communications*, 180, 2009.

[17] J.-F. Arguin et al. Search for anomalous production of prompt like-sign lepton pairs and constraints on physics beyond the Standard Model. `https://cds.cern.ch/record/1494589`, 2012. ATLAS Internal Note (only accessible by ATLAS members). Retrieved January 6th, 2014.

[18] N. Arkani-Hamed et al. The Minimal Moose for a Little Higgs. *JHEP*, 208(21), 2002.

[19] ATLAS Collaboration. *ATLAS computing: Technical Design Report*. CERN, 2005.

[20] ATLAS Collaboration. Expected Performance of the ATLAS Experiment: Detector, Trigger and Physics. *CERN-OPEN-2008-020*, 2008.

[21] ATLAS Collaboration. The ATLAS experiment at the CERN Large Hadron Collider. *JINST*, 3, 2008.

[22] ATLAS Collaboration. Studies of the performance of the ATLAS detector using cosmic-ray muons. *The Europiean Physical Journal C*, 71(1593), 2011. arXiv:1011.6665 [physics.ins-det].

[23] ATLAS Collaboration. Observation of a New Particle in the Search for the Standard Model Higgs Boson with the ATLAS Detector at the LHC. *Physics Letters B*, 716(1):1–29, 2012.

[24] ATLAS collaboration. Search for anomalous production of prompt like-sign lepton pairs at sqrt(s) = 7 TeV with the ATLAS detector. *JHEP*, 1212(007), 2012. arXiv:1210.4538 [hep-ex].

[25] ATLAS Collaboration. Measurements of Higgs boson production and couplings in diboson final states with the ATLAS detector at the LHC. *Physics Letters B*, 726:88–119, 2013. arXiv:1307.1427.

[26] ATLAS Collaboration. Evidence for the spin-0 nature of the Higgs boson using ATLAS data. *Physics Letters B*, 726:120–144, 2013. arXiv:1307.1432.

[27] ATLAS collaboration. Search for anomalous production of prompt same-sign lepton pairs and constraints on physics beyond the Standard Model with sqrt(s) = 8 TeV data. `https://cds.cern.ch/record/1527118`, 2013. ATLAS Internal Note (only accessible by ATLAS members). Retrieved January 6th, 2014.

[28] ATLAS Statistics Forum. The CL_s method: information for conference speakers. `https://twiki.cern.ch/twiki/pub/AtlasProtected/StatisticsTools/CLsInfo.pdf`, 2011. Only accessible by ATLAS members.

[29] R. Barnett, J. Gunion, and H. Haber. Discovering supersymmetry with like sign dileptons. *Physics Letters B*, 315:349–354, 1993. arXiv:hep-ph/9306204.

[30] J. Beringer et al. Particle Data Group. *Physical Review D*, 86, 2012.

[31] G. Bernardi, M. Carena, and T. Junk. Higgs Bosons: Theory and Searches. `http://pdg.lbl.gov/2008/reviews/higgs_s055.pdf`, 2007. Retrieved January 23rd, 2014.

[32] A. Bocci et al. Electron-performance measurements with the ATLAS detector using the 2011 LHC proton-proton collision data. `https://cds.cern.ch/record/1612217`, 2013. ATLAS Internal Note (only accessible by ATLAS members). Retrieved January 6th, 2014.

[33] N. Boelaert. *Dijet angular distributions in proton-proton collisions at* $\sqrt{s} = 7$ *TeV and* $\sqrt{s} = 8$ *TeV*. PhD thesis, Lund University, 2010.

[34] O. S. Brüning et al. LHC Design Report. `https://ab-div.web.cern.ch/ab-div/Publications/LHC-DesignReport.html`, 2004. Retrieved January 6th, 2014.

[35] CMS Collaboration. Observation of a new boson at a mass of 125 GeV with the CMS experiment at the LHC. *Physics Letters B*, 716(1):30–61, 2012.

[36] G. Cowan. Statistics for Searches at the LHC. 2013. arXiv:1307.2487 [hep-ex].

[37] K. Cranmer. Practical Statistics for the LHC. `http://indico.hep.lu.se//getFile.py/access?resId=0&materialId=3&confId=1255`. ATLAS Internal Note (only accessible by ATLAS members). Retrieved January 6th, 2014.

[38] K. Cranmer et al. HistFactory: A tool for creating statistical models for use with RooFit and RooStats. *CERN-OPEN-2012-016*, 2012.

[39] L. Evans and P. Bryant (editors). LHC Machine. *Journal of instrumentation*, 3, 2008.

[40] S. Frixione and B. Webber. Matching NLO QCD computations and parton shower simulations. *JHEP*, 0206(029), 2002. [hep-ph/0204244].

[41] Y. Fukuda et al. Evidence for oscillation of atmospheric neutrinos. *Physical Review Letters*, 81:1562–1567, 1998. arXiv:hep-ex/9807003.

[42] D. S. Gorbunov and V. A. Rubakov. *Introduction to the Theory of the Early Universe: Hot Big Bang Theory*. World Scientific Publishing Co. Pte. Ltd., 2011.

[43] J. Groth-Jensen. *Luminosity determination and simulation of the LUCID detector at the ATLAS experiment*. PhD thesis, Lund University, 2010.

[44] J. F. Gunion, J. Grifols, A. Mendez, B. Kayser, and F. Olness. Higgs Bosons in Left-Right Symmetric Models. *Phys. Rev. D*, 40:1546, 1989.

[45] M. Hostettler and G. Papotti. Observations from LHC proton-proton physics operation. `http://indico.cern.ch/getFile.py/access?contribId=80&sessionId=13&resId=0&materialId=paper&confId=189544`, 2013. Retrieved January 6th, 2014.

[46] W. Lampl and S. Laplace et al. Calorimeter Clustering Algorithms: Description and Performance. *ATL-LARG-PUB-2008-002*, 2008.

[47] P. Langacker. *The Standard Model and Beyond*. CRC Press, 2010.

[48] S. Laplace and J.-B. de Vivie et al. Calorimetric isolation and pile-up. *ATL-COM-PHYS-2012-467*, 2012. Only accessible by ATLAS members.

[49] B. R. Martin and G. Shaw. *Particle Physics*. John Wiley & Sons, 3rd edition, 2008.

[50] L. Moneta et al. The RooStats Project. 2011. arXiv:1009.1003 [physics.data-an].

[51] G. Ranucci. The profile likelihood ratio and the look elsewhere effect in high energy physics. *Nuclear Instruments and Methods in Physics Research A*, 661(1):77–85, 2012.

[52] A. L. Read. Presentation of search results: the CL_s technique. *Journal of Physics G: Nuclear and Particle Physics*, 28(10), 2002.

[53] G. Senjanovic and R. N. Mohapatra. Exact left-right symmetry and spontaneous violation of parity. *Physical Review D*, 12:1502, 1975.

[54] M. H. Seymour and M. Marx. Monte Carlo Event Generators. 2013. arXiv:1304.6677 [hep-ph].

[55] S. Shmatov. Search for extra dimensions with ATLAS and CMS detectors at the LHC. `http://arxiv.org/pdf/0707.0470.pdf`, 2007. Retrieved January 6th, 2014.

[56] T. Sjöstrand. PYTHIA. `http://home.thep.lu.se/~torbjorn/Pythia.html`, 2013. Retrieved January 6th, 2014.

[57] The ROOT team. PROOF. `http://root.cern.ch/drupal/content/proof`, 2013. Retrieved January 6th, 2014.

[58] TOTEM Collaboration. A luminosity-independent measurement of the proton-proton total cross-section at $\sqrt{s} = 8$ TeV. *Physical Review Letters*, 111(1), 2012.

[59] G. Unal and J. Boyd. ATLAS EXPERIMENT - Public Results: Luminosity Public Results. `https://twiki.cern.ch/twiki/bin/view/AtlasPublic/LuminosityPublicResults`, August 2012. Retrieved January 6th, 2014.

[60] W. Verkerke and D. Kirkby. The RooFit toolkit for data modelling. 2003. arXiv:physics/0306116 [physics.data-an].

Appendix A

Limits for positive and negative lepton pairs separately

Table A.1: 95% C.L. upper limit on the number of positive lepton pairs due to non-SM physics in each lepton channel and mass bin. The 1σ and 2σ bands are given on the expected limit. Observed limits are based on dummy numbers.

	95% C.L. upper limit [number of events]					
	e^+e^+		$e^+\mu^+$		$\mu^+\mu^+$	
Mass range	expected	observed	expected	observed	expected	observed
$M > 15$ GeV	$273.08^{+97.31+}_{-49.94-}{}^{+211.81}_{-95.02}$	351.65	$478.40^{+124.00+}_{-133.50-}{}^{+276.43}_{-200.94}$	525.88	$71.61^{+24.55+}_{-20.41-}{}^{+58.88}_{-31.68}$	31.97
$M > 100$ GeV	$124.92^{+59.02+}_{-31.31-}{}^{+118.84}_{-47.69}$	246.47	$192.07^{+65.90+}_{-34.90-}{}^{+123.23}_{-69.82}$	238.66	$36.03^{+14.48+}_{-11.05-}{}^{+32.01}_{-18.04}$	31.58
$M > 200$ GeV	$47.07^{+23.11+}_{-11.62-}{}^{+46.11}_{-16.88}$	82.25	$44.87^{+16.79+}_{-12.43-}{}^{+36.27}_{-18.30}$	50.45	$17.01^{+6.62+}_{-4.99-}{}^{+14.21}_{-7.55}$	9.79
$M > 300$ GeV	$25.00^{+9.32+}_{-6.45-}{}^{+21.94}_{-9.26}$	36.14	$20.35^{+8.49+}_{-5.02-}{}^{+17.32}_{-9.96}$	23.19	$9.69^{+3.88+}_{-2.79-}{}^{+8.72}_{-4.64}$	7.32
$M > 400$ GeV	$18.72^{+4.81+}_{-4.53-}{}^{+12.49}_{-6.22}$	19.44	$13.64^{+6.19+}_{-3.23-}{}^{+14.38}_{-5.00}$	13.83	$6.10^{+2.89+}_{-1.23-}{}^{+5.87}_{-3.06}$	5.33
$M > 500$ GeV	$7.81^{+2.68+}_{-1.90-}{}^{+6.94}_{-2.68}$	9.31	$8.74^{+4.43+}_{-2.34-}{}^{+11.25}_{-3.36}$	7.77	$4.03^{+2.16+}_{-0.94-}{}^{+4.91}_{-1.17}$	3.58

Table A.2: 95% C.L. upper limit on the number of negative lepton pairs due to non-SM physics in each lepton channel and mass bin. The 1σ and 2σ bands are given on the expected limit. Observed limits are based on dummy numbers.

	95% C.L. upper limit [number of events]					
	e^-e^-		$e^-\mu^-$		$\mu^-\mu^-$	
Mass range	expected	observed	expected	observed	expected	observed
$M > 15$ GeV	$239.70^{+90.07+}_{-56.31-}{}^{+203.51}_{-89.34}$	229.94	$418.64^{+102.81+}_{-98.14-}{}^{+255.78}_{-128.32}$	339.72	$63.83^{+23.98+}_{-17.97-}{}^{+52.54}_{-26.13}$	83.62
$M > 100$ GeV	$145.55^{+50.73+}_{-39.04-}{}^{+116.16}_{-64.59}$	119.24	$164.74^{+47.55+}_{-45.15-}{}^{+104.20}_{-57.01}$	146.87	$30.75^{+11.50+}_{-7.89-}{}^{+26.76}_{-14.54}$	43.05
$M > 200$ GeV	$52.78^{+20.09+}_{-14.89-}{}^{+45.74}_{-24.06}$	34.59	$46.09^{+15.48+}_{-13.81-}{}^{+34.29}_{-16.29}$	38.52	$14.00^{+4.57+}_{-3.77-}{}^{+11.24}_{-6.41}$	17.05
$M > 300$ GeV	$24.86^{+10.30+}_{-6.62-}{}^{+22.75}_{-12.27}$	18.88	$20.41^{+9.13+}_{-5.42-}{}^{+18.25}_{-10.12}$	15.16	$7.58^{+2.46+}_{-1.72-}{}^{+6.79}_{-3.19}$	11.18
$M > 400$ GeV	$16.61^{+4.69+}_{-3.97-}{}^{+11.52}_{-4.50}$	17.36	$13.06^{+5.76+}_{-4.15-}{}^{+14.17}_{-5.05}$	8.72	$4.24^{+1.94+}_{-0.82-}{}^{+4.30}_{-1.29}$	6.73
$M > 500$ GeV	$12.38^{+4.51+}_{-1.27-}{}^{+9.17}_{-3.37}$	12.57	$8.34^{+3.84+}_{-2.46-}{}^{+9.73}_{-4.46}$	5.80	$3.32^{+0.68+}_{-0.11-}{}^{+2.31}_{-0.17}$	4.09

Table A.3: 95% C.L. upper limit on the fiducial cross-section of non-SM physics in each lepton channel and mass bin for positive lepton pairs. The 1σ and 2σ bands are given on the expected limit. Observed limits are based on dummy numbers.

	95% C.L. upper limit [fb]					
	e^+e^+		$e^+\mu^+$		$\mu^+\mu^+$	
Mass range	expected	observed	expected	observed	expected	observed
$M > 15$ GeV	$31.02^{+11.06+}_{-5.67-}{}^{+24.06}_{-10.79}$	39.95	$42.73^{+11.08+}_{-11.92-}{}^{+24.69}_{-17.95}$	46.97	$5.96^{+2.04+}_{-1.70-}{}^{+4.90}_{-2.64}$	2.66
$M > 100$ GeV	$14.19^{+6.70+}_{-3.56-}{}^{+13.50}_{-5.42}$	28.00	$17.16^{+5.89+}_{-3.12-}{}^{+11.01}_{-6.24}$	21.32	$3.00^{+1.21+}_{-0.92-}{}^{+2.67}_{-1.50}$	2.63
$M > 200$ GeV	$5.35^{+2.63+}_{-1.32-}{}^{+5.24}_{-1.92}$	9.34	$4.01^{+1.50+}_{-1.11-}{}^{+3.24}_{-1.63}$	4.51	$1.42^{+0.55+}_{-0.42-}{}^{+1.18}_{-0.63}$	0.82
$M > 300$ GeV	$2.84^{+1.06+}_{-0.73-}{}^{+2.49}_{-1.05}$	4.11	$1.82^{+0.76+}_{-0.45-}{}^{+1.55}_{-0.89}$	2.07	$0.81^{+0.32+}_{-0.23-}{}^{+0.73}_{-0.39}$	0.61
$M > 400$ GeV	$2.13^{+0.55+}_{-0.51-}{}^{+1.42}_{-0.71}$	2.21	$1.22^{+0.55+}_{-0.29-}{}^{+1.28}_{-0.45}$	1.24	$0.51^{+0.24+}_{-0.10-}{}^{+0.49}_{-0.25}$	0.44
$M > 500$ GeV	$0.89^{+0.30+}_{-0.22-}{}^{+0.79}_{-0.30}$	1.06	$0.78^{+0.40+}_{-0.21-}{}^{+1.00}_{-0.30}$	0.69	$0.34^{+0.18+}_{-0.08-}{}^{+0.41}_{-0.10}$	0.30

Table A.4: 95% C.L. upper limit on the fiducial cross-section of non-SM physics in each lepton channel and mass bin for negative lepton pairs. The 1σ and 2σ bands are given on the expected limit. Observed limits are based on dummy numbers.

	95% C.L. upper limit [fb]					
	e^-e^-		$e^-\mu^-$		$\mu^-\mu^-$	
Mass range	expected	observed	expected	observed	expected	observed
$M > 15$ GeV	$27.23^{+10.23+}_{-6.40-}{}^{+23.12}_{-10.15}$	26.12	$37.39^{+9.18+}_{-8.77-}{}^{+22.85}_{-11.46}$	30.34	$5.32^{+2.00+}_{-1.50-}{}^{+4.38}_{-2.18}$	6.96
$M > 100$ GeV	$16.54^{+5.76+}_{-4.44-}{}^{+13.20}_{-7.34}$	13.55	$14.71^{+4.25+}_{-4.03-}{}^{+9.31}_{-5.09}$	13.12	$2.56^{+0.96+}_{-0.66-}{}^{+2.23}_{-1.21}$	3.59
$M > 200$ GeV	$6.00^{+2.28+}_{-1.69-}{}^{+5.20}_{-2.73}$	3.93	$4.12^{+1.38+}_{-1.23-}{}^{+3.06}_{-1.46}$	3.44	$1.17^{+0.38+}_{-0.31-}{}^{+0.94}_{-0.53}$	1.42
$M > 300$ GeV	$2.82^{+1.17+}_{-0.75-}{}^{+2.58}_{-1.39}$	2.15	$1.82^{+0.82+}_{-0.48-}{}^{+1.63}_{-0.90}$	1.35	$0.63^{+0.21+}_{-0.14-}{}^{+0.57}_{-0.27}$	0.93
$M > 400$ GeV	$1.89^{+0.53+}_{-0.45-}{}^{+1.31}_{-0.51}$	1.97	$1.17^{+0.51+}_{-0.37-}{}^{+1.27}_{-0.45}$	0.78	$0.35^{+0.16+}_{-0.07-}{}^{+0.36}_{-0.11}$	0.56
$M > 500$ GeV	$1.41^{+0.51+}_{-0.14-}{}^{+1.04}_{-0.38}$	1.43	$0.75^{+0.34+}_{-0.22-}{}^{+0.87}_{-0.40}$	0.52	$0.28^{+0.06+}_{-0.01-}{}^{+0.19}_{-0.01}$	0.34

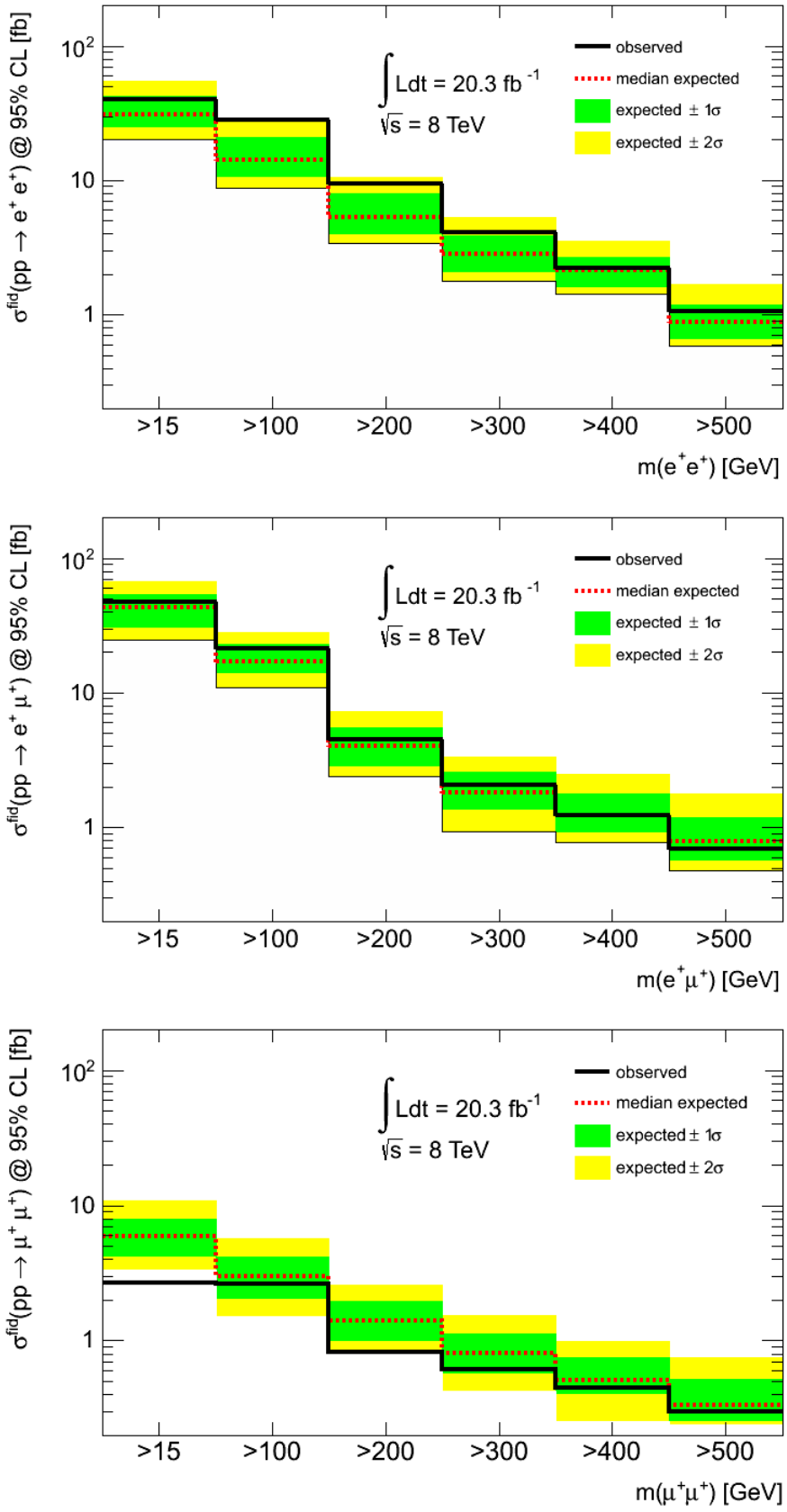

Figure A.1: 95% C.L. upper limit on the fiducial cross-section of non-SM physics in each lepton channel and mass bin for positive lepton pairs. The 1σ and 2σ bands are given on the expected limit. Observed limits are based on dummy numbers.

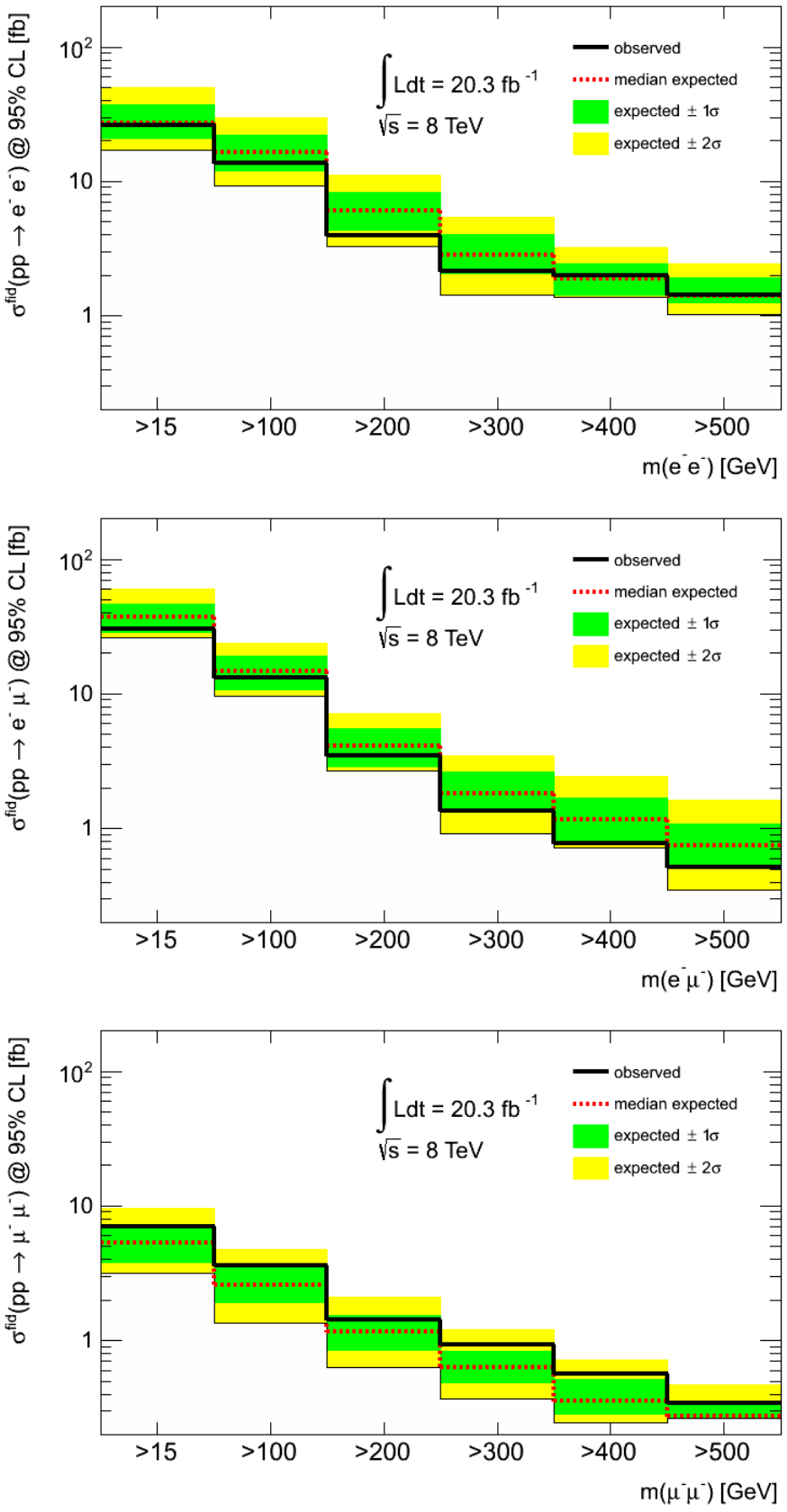

Figure A.2: 95% C.L. upper limit on the fiducial cross-section of non-SM physicsin each lepton channel and mass bin for negative lepton pairs. The 1σ and 2σ bands are given on the expected limit. Observed limits are based on dummy numbers.